MnDOT Contract, No. 1003325, Work Order No. 56

NRRA Long-term Research Project

Performance Benefits of Fiber-reinforced Thin Concrete Pavement and Overlays

Task 4: Analysis to Determine Contribution of Fibers in Mitigating Joint Faulting

Prepared by:

Souvik Roy, Manik Barman, Amarjeet Tiwari, UMD

and

Tom Burnham, Minnesota Department of Transportation

UMD

UNIVERSITY OF MINNESOTA DULUTH

Driven to Discover

DEPARTMENT OF TRANSPORTATION

2020

TABLE OF CONTENTS

LIST OF FIGURES

LIST OF TABLES

CHAPTER 1: **INTRODUCTION**

The Minnesota Department of Transportation (MnDOT) constructed several fiber reinforced concrete (FRC) test cells at MnROAD in 2017. MnROAD test facility is located on westbound I-94 near Otsego, northwest of the Twin Cities metropolitan area. These cells were constructed as a part of a National Road Research Alliance (NRRA) funded long-term research study on fiber reinforced concrete pavements. The main research objective behind constructing these cells is to identify and quantify the contribution of synthetic structural fibers in mitigating different distresses that typically occur in thin and ultra-thin concrete pavements and overlays. A total of eight cells were constructed, among which seven cells were constructed with FRC, and one control cell was constructed with plain cement concrete (Cell 506). Cells 139 and 239 were constructed as ultra-thin (3-inch thick) and thin (4-inch thick) concrete pavement on granular gravel base (designed to mimic a typical city street design). An enhanced fiber dosage (8 lb/cy, 30% residual strength ratio (RSR)) was used in these two cells. Cells 705 and 805 were constructed as thin unbonded concrete overlays on an existing concrete pavement, with varying panel sizes; a more typical fiber dosage (5 lb/cy, 20% RSR) was used in these two cells. Cells 506 through 806 were constructed as thin concrete pavements on an unstabilized gravel base, with varying fiber dosages (0 to 11.7 lb/cy). This report presents the works performed under the scope of Task 4, which characterizes the contribution of structural synthetic fibers in mitigating transverse joint faulting.

Faulting measurements were performed at different seasons in 2017, 2018, and 2019. The joint performance measured by a falling weight deflectometer (FWD) device was analyzed to investigate the influence of fibers on the joint load transfer efficiency, load side displacement, differential deflection, and void accumulation under the slab. All the collected data were analyzed and furnished in this report with an objective to identify and quantify the contribution of different pavement variables, including fibers. Once the significant variables were identified using the statistical tool Minitab, fault prediction equations were developed. These equations can be used to predict the faulting of thin and ultra-thin fiber reinforced concrete pavements.

CHAPTER 2: **LITERATURE REVIEW**

Faulting is defined as the difference in the elevation between the two adjacent slabs across transverse joints in concrete pavements. Faulting affects drivers safety and decreases smoothness of the ride (Byrum and Perera, 2005) [1]. The National Cooperative Highway Research Program (NCHRP) report for Transverse Joint Faulting (ARA, 2003) [2] summarized different variables that influence the faulting and were considered in various faulting predicting models (Table 1). It appears that equivalent single axle load (ESAL), drainage coefficient, modulus of subgrade reaction, slab thickness, transverse joint spacing, and shoulder types are some influential variables for faulting.

Table 1: Variables considered in joint faulting models in different studies by ARA, 2003

Variable	SHRP P-020 (1984)[3]	RPPR (1997)[4]	ACPA (1994)[5]	NAPCOM (1997)[6]	LTPP Data Analysis (1997)[7]	PaveSpec 3.0 (2000)[8]
Age	X	X				
80-kN (18-kip) ESALs	X	X			X	X
Axle load repetitions			X	X		
Drainage type	X	X				X
AASHTO drainage coefficient, C_d		X		X	X	
PCC slab thickness		X	X	X	X	X
PCC modulus of elasticity		X		X	X	X
Modulus of subgrade reaction (k-value)	X	X	X	X	X	X
Base type		X		X	X	X
Shoulder type	X	X		X	X	X
Transverse joint spacing	X	X	X	X	X	X
Dowel diameter	X	X			X	X

Jung and Zollinger (2011)[9] developed a laboratory-based mechanistic-empirical model for predicting faulting for jointed plain concrete pavement (JPCP), focusing on the bonding at the interface, erosion of the granular layer and equivalent single axle loads (ESALs). Figure 1 depicts the cumulative accumulation of faulting with ESALs, divided into different regions based on the interface bonding condition.

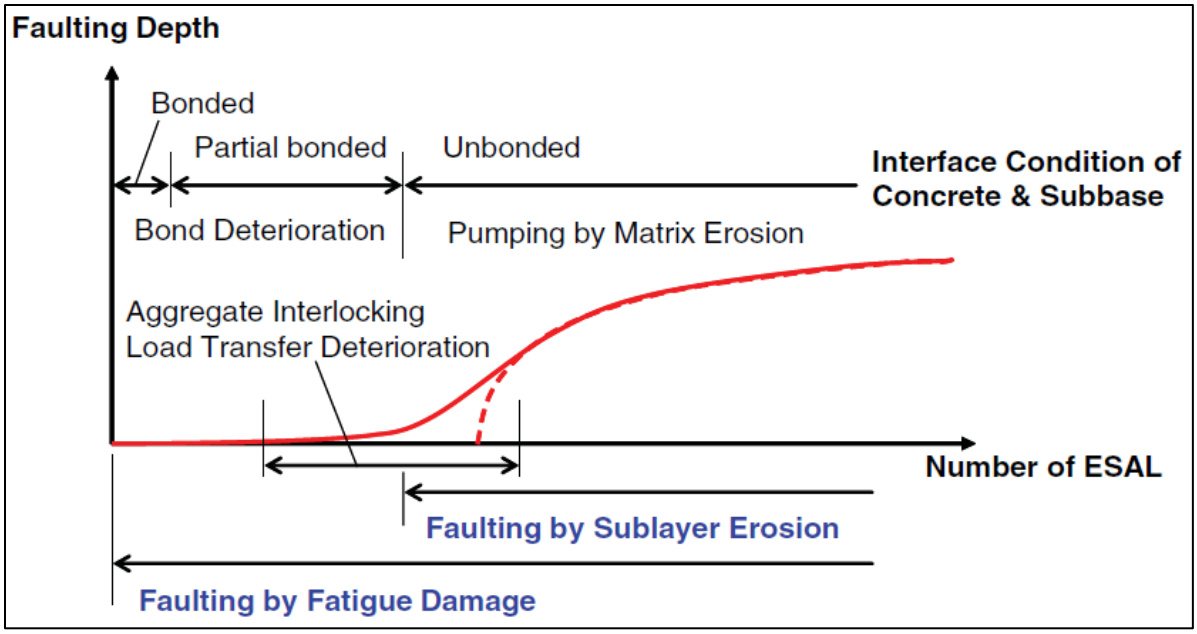

Figure 1: Faulting accumulation as a function of ESALs and interface bonding (Jung & Zollinger, 2011)

Equation (1) provides the basic faulting model developed in the Jung and Zollinger (2011) study. It predicts the magnitude of faulting depth at a given ESAL value, based on the ultimate average faulting depth and erosion ratio. The model proposed in this study was calibrated with laboratory test results and data from the Long Term Pavement Performance (LTPP) database.

$$fault_i = fault_0 * e^{-\left(\frac{\rho}{Ni-Ne}\right)^{\alpha}} \quad (1)$$

Where,

$fault_i$	= average faulting depth for a given ESAL. (m or in.);
$fault_0$	= ultimate average faulting depth (m or in.);
$e^{-\left(\frac{\rho}{Ni-Ne}\right)^{\alpha}}$	= erosion ratio at the given number of ESALs;
ρ	= calibration erosion coefficient based on local performance;
N_i	= number of ESAL traffic contributing to erosion;
N_e	= calibration coefficient represents the number of wheel loads (or time) to incur layer debonding of slab and subbase and to initiate erosion;
α	= composite calibration rate coefficient based on field and laboratory performance

Chen and Lytton (2019) improvised the Jung and Zollinger (2011) model and modified the same with a sigmoidal-shape model, as presented in Equation (2) [10]. This model has predominantly two stages. The first stage represents a smooth and gradual increment of faulting depth caused by the plastic deformation of the underlying layers. The second stage represents a rapid increase of faulting, indicating erosion of underlying layers due to variable weather conditions and moisture cycles. In the Chen and Lytton (2019)

model, the faulting depth is predicted based on the number of days after the pavement construction date (N), the number of days before faulting initiates (N_0), number of days to failure as a result of erosion (N_∞), and some other model coefficients. This model was also validated with the faulting data from the LTPP database; as shown in Figure 2. The authors noted that the model predicted faulting depth compares well with the faulting data from the LTPP database, with an R^2 value of 0.95.

$$f = \rho_e * [\ln\left(\frac{N\infty}{N - N0}\right]^{\frac{1}{\beta e}}) \quad (2)$$

Where f = faulting depth.
ρ_e and β_e are model coefficients.

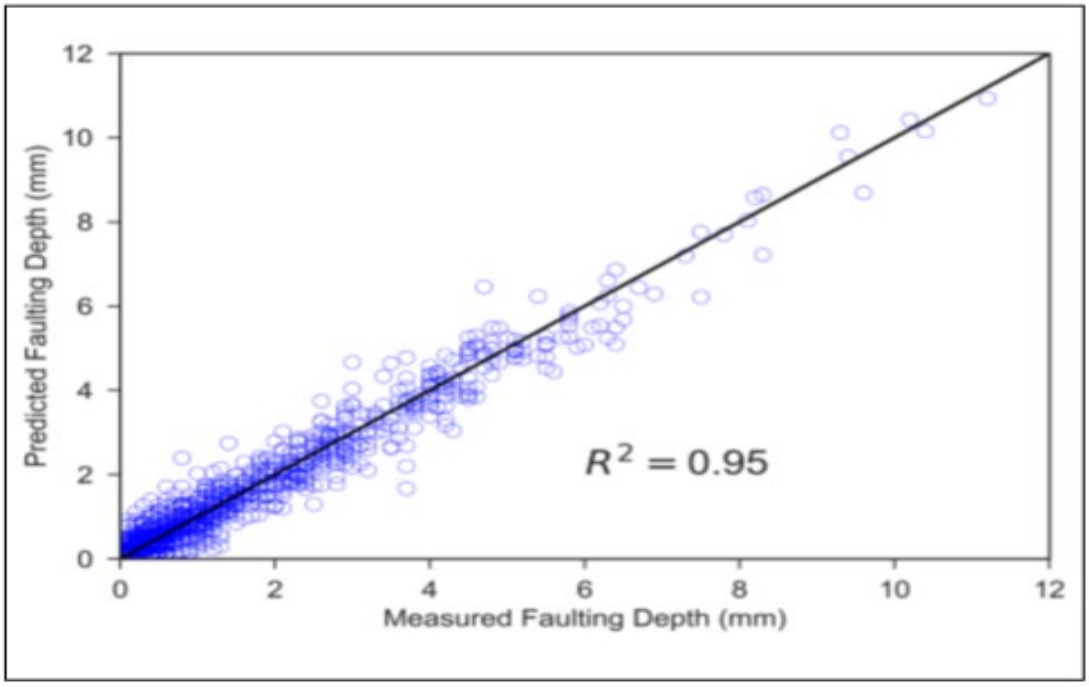

Figure 2: Comparison of measured versus predicted faulting depth in Chen and Lytton (2019) model

Khazanovich et al. (2019) [11] developed a faulting model for unbonded concrete overlays. The study included laboratory testing, MnROAD performance data analysis, and a finite element analysis (using ISLAB). This study provided a model for incremental monthly joint faulting as a function of base freezing index and differential energy density (DE). DE is a function of joint spacing, aggregate interlock, load transfer provided by the shoulder, interlayer property, etc. The interlayer property in the finite element modeling was assumed as a bed of springs between two plates; the spring stiffness was represented by the Totsky layer coefficient. Equations (3) and (4) show the faulting model as proposed in Khazanovich et al. (2019). An important aspect of this study was characterizing the base erosion, represented by a parameter called basin sum deflection. The basin was considered as a 2 feet x 6 feet imaginary rectangular area along the wheel path that is heavily influenced by traffic load. The basin sum

deflection was defined as the difference in deflection values between approach and leave slabs for the basin area.

$$Fault_i = Fault_{i-1} + \Delta Fault_i \quad (3)$$

$$\Delta Fault_i = (C_3 + C_4 * FR^{0.25}) * (F_{i-1} - Fault_{i-1})^2 * C_8 * DE_i \quad (4)$$

Where,

$Fault_i$= Maximum mean transverse joint faulting for the month i (in.)

$Fault_{i-1}$= Mean joint faulting at the beginning of the month i (in.)

$\Delta Fault_i$= Incremental monthly change in the transverse joint faulting during the month i (in.)

FR= Base freezing index and DE_i= Differential energy density accumulated for the month i.

CHAPTER 3: **MnROAD TEST CELLS**

3.1 DESCRIPTION OF THE TEST SECTIONS

This section presents the design and construction details of the MnROAD test cells constructed under the scope of this project. Table 2 presents the design details, and Figure 3 shows the location of cells in MnROAD test facility. Table 3 shows the construction time of different cells. Figure 4 to Figure 6 shows the section properties of all the 7 FRC cells and one control cell, 506.

Cells 705 and 805 were constructed as overlays on an existing concrete pavement, which was constructed in 1993. All other cells were constructed as new pavement on a granular aggregate base. Cell 506 was constructed as the control cell with no fibers in it. Cells 139 and 239 were 3-inch and 4-inch thick, respectively, with enhanced fiber dosage, as noted in Table 2. Fiber dosages were decided either based on the residual strength ratio (RSR) or fiber volume fraction. The RSR, determined in accordance with ASTM 1609 [12], is the ratio of flexural load at 120 mils (3 mm) mid-span deflection to the peak flexural load.

Cells 506, 706, and 806 were 5-inch thick with varying fiber dosage as described in the Table 2. The Cell 606 was also planned to be constructed as 5-inch thick, but the thickness measured at multiple locations revealed that the as-built thickness averages 6-inches for this cell.

A photograph of the fiber used in the construction is shown in Figure 7. The properties of this fiber can be found in Task 2B report for this project (Barman et al., 2020) [13].

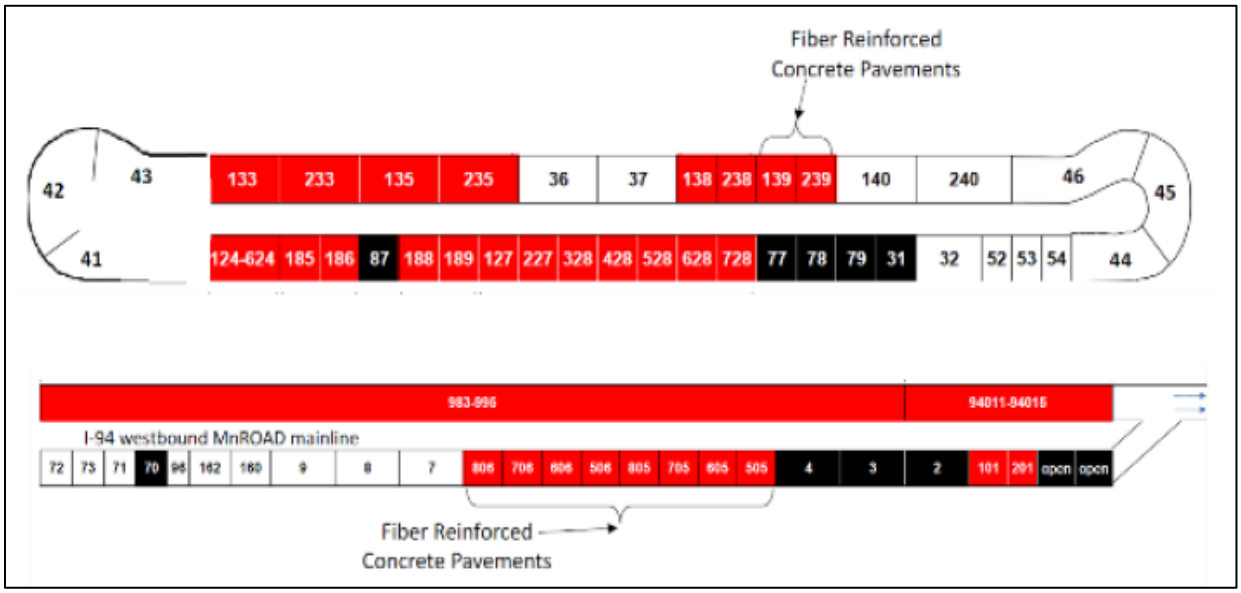

Figure 3: Location of the 2017 FRC research cells at the MnROAD test facility (MnDOT, 2018)

Table 2: Summary of the 2017 NRRA MnROAD test cells constructed for FRC study (MnDOT, 2018)

Cell number	Length (ft)	Pavement/ overlay Type	Underlying layer (constr. year)	Type of concrete/ fiber dosage*	Panel size W ft x L ft	Panel thickness (inch)
506	144	Thin pavement on gravel base	11 in. class 5Q aggregate base (2017)	*Plain concrete*	6 x 6	5
606**	138			*FRC/ standard*		
706				*FRC/ enhanced*		
806				*FRC/ high*		
139	270	Ultra-thin Pavement on gravel base	6 in. class 5 aggregate base (2017)	FRC/ enhanced	6 x 6	*3*
239	273	Thin Pavement on gravel base			6 x 6	*4*
705	144	Thin unbonded overlay on concrete pavement (w/fabric interlayer)	Concrete (1993)	FRC/ standard	*Driving: 14 x 12 Passing: 12 x 12*	5
805	124				*Driving: 6 x 12 and 8 x 12 Passing: 6 x 12 and 6 x 12*	5

** Fiber dosages: standard - corresponding to 20% residual strength ratio (ASTM C1609); enhanced - corresponding to 30% residual strength ratio (ASTM C1609); high – corresponding to 0.75 fibers volume fraction.*

*** Even though the design thickness was 5 inches, the actual measured thickness was found to be 6 inches*

Table 3: Paving time and date of the 2017 MnROAD FRC cells (MnDOT, 2018)

CELL	Date	Approximate Time
139	7/17/2017	9:15:00 AM
239	7/17/2017	9:15:00 AM
506	6/26/2017	9:20:00 AM
606	6/27/2017	9:15:00 AM
706	6/29/2017	8:45:00 AM
806	6/30/2017	8:00:00 AM
705	9/5/2017	2:00:00 PM
805	9/5/2017	3:00:00 PM

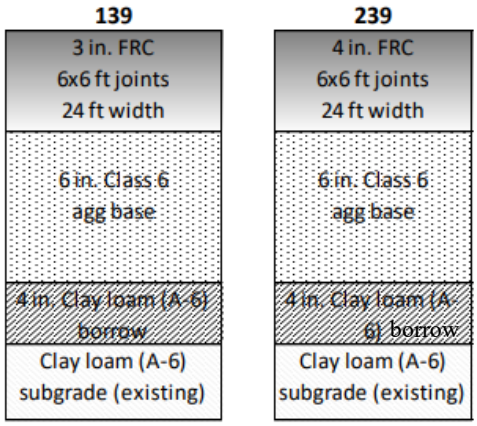

Figure 4: Section details for Cells 139 & 239 (MnDOT, 2018)

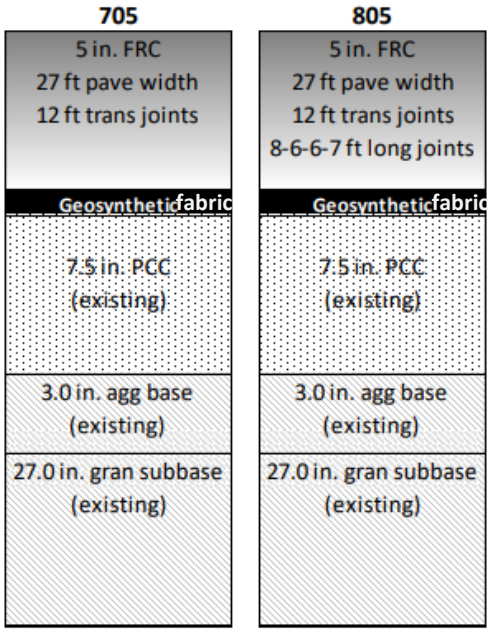

Figure 5: Section details for Cells 705 and 805 (MnDOT, 2018)

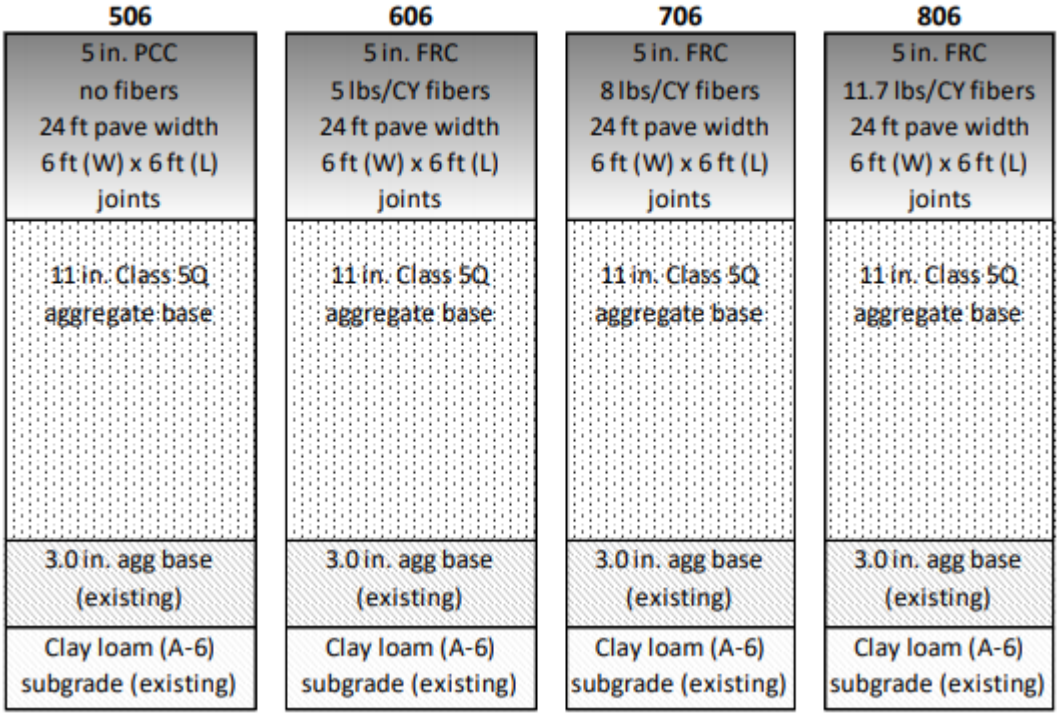

Figure 6: Section details for cells 506, 606, 706 and 806 (MnDOT, 2018)

Figure 7: Fibers used in the NRRA FRC study, 2017

3.2 TRAFFIC LOADING

MnROAD test facility is composed of two different test track segments. Cells 139 and 239 were constructed on the low volume test loop, which has two lanes, commonly referred to as the inside and outside lane. The inside lane is exposed to traffic loads; whereas, the outside lane is reserved for studying

the influence of the environmental loads alone on the pavement. The traffic load on the LVR section is provided by a 356-kN, 5-axle, tractor/trailer combination [14], which averages approximately 70 laps per day, equivalent to 30,000 to 40,000 concrete pavement ESALs per year depending on the thickness of the test cells. Until April 24, 2019, the ESAL calculated for Cell 139 was 86,625, and that for the Cell 239 was 66,089.

Cells 506 to 806, and the two overlay cells (Cells 705 and 805), were constructed on the high traffic volume segment of MnROAD, which consists of two lanes running parallel to the original westbound interstate highway I-94. These two lanes receive live traffic diverted off of westbound I-94 approximately 75 percent of the time. The test cells in this study therefore received about 2.5 million ESALs by the end of October 2019 (Approximately 1 million ESALs per year).

3.3 MATERIAL PROPERTIES

3.3.1 CONCRETE MIX DESIGN AND OTHER PROPERTIES

Four different types of concrete mixes [15] were used for the present study. They are discussed as follows:

1. MR-3A21FC: This mix had zero fiber content and was used in the control Cell 506.

2. MR-3A21F1: This mix has a "standard" fiber dosage (i.e., with 20% RSR, 5 lb/cy fiber dosage). Cells 705, 805, and 606 contained this concrete mix. The "standard" dosage comes from the current specifications developed by the Illinois DOT.

3. MR-3A21F2: This mix has an "enhanced" fiber dosage (i.e., with 30% RSR, 8 lb/cy fiber dosage). This mix was used in Cells 139, 239, and 706.

4. MR-3A21F3: This particular mix, used in Cell 806 alone, had the highest practical fiber dosage (0.75% fiber volume fraction, 11.7 lb/cy fiber dosage) as determined by a recently completed MnDOT sponsored study conducted by the University of Minnesota-Duluth (Barman and Hansen, 2018) [16].

Table 4 shows the mix proportions for the abovementioned four different types of concrete mixes.

Table 4: Mix design information for FRC cells (MnROAD, 2018)

Mix/Cell	Air (%)	Water (lbs)	Cement (lbs)	Fly ash (lbs)	Fly ash (%)	W/C Ratio	FA #1 (lbs)	CA #1 (lbs)	Fibers (lb/cy)	Fibers (% of conc. vol.)	Target RSR (%)	Slump range (in.)
MR-3A21FC/ 506	7.0	239	400	170	30	0.42	1222	1798	0	0	0	0.5-3
MR-3A21F1/ 705,805,606		248	413	177			1204	1773	5	0.33	20	
MR-3A21F2/ 139,239,706		252	420	180			1196	1761	8	0.52	30	
MR-3A21F3/ 806		258	430	185			1184	1743	11.66	0.75	NA	

Table 5 presents the test results of beams prepared at the project site for the ASTM C1609 test. The average 28-day residual strength for the concrete used in Cells 606, 706, and 806 were 124, 156, and 254 psi, respectively. The average 28-day residual strength for Cells 139 and 239 was 185 psi, and it was 116.53 psi for Cells 705 and 805. The 28-day MORs for Cell 506, 606, 706, and 806 were 650, 635, 675, and 680 psi, respectively. The same for Cells 139 and 239 was 610 psi, and it was 542 psi for Cells 705 and 805. The other relevant fresh and hard concrete test results, including the ASTM C1609 test results for all the cells, are provided in the Appendix.

Table 5: Measured properties of concretes used in the FRC research cells.

Cell number	Hardened concrete properties		
	28-day MOR (psi)	28-day residual strength (psi)	28-day RSR (%)
139	610	185	30.4
239			
705	542	116	21.5
805			
506	650	-	-
606	640	124	19.4
706	680	156	23.0
806	680	254	37.4

3.3.2 BASE LAYER PROPERTIES

Base materials used in the FRC cells were not tested under the scope of this study. Resilient modulus values for similar base materials were collected from MnDOT pavement design manual (2007)[17]. Table 6 shows the resilient modulus values for different types of base and subbase materials for different seasons. Resilient modulus results for MnDOT Class 5 aggregates were used for this study.

Table 6: MnDOT base/subbase layer resilient modulus values for various aggregate class (MnDOT, 2007)

Mn/DOT Material Classification	Granular Equivalent (G.E. Value)	Resilient Modulus by Season									
		Early Spring		Late Spring		Summer		Fall		Winter	
		MPa	ksi	MPa	ksi	MPa	ksi	MPa	ksi	MPa	ksi
CLASS 7 (Mn/DOT Spec. 3138)	1.0	62	9	124	18	207	30	228	33	350	50
CLASS 6 (Mn/DOT Spec. 3138)	1.0	71	10	141	20	236	34	259	38	350	50
CLASS 5 (Mn/DOT Spec. 3138)	1.0	62	9	124	18	207	30	228	33	350	50
CLASS 4 (Mn/DOT Spec. 3138)	0.75	58	8.3	115	16.7	192	27.8	211	30.6	350	50
CLASS 3 (Mn/DOT Spec. 3138)	0.75	58	8.3	115	16.7	192	27.8	211	30.6	350	50
SELECT GRANULAR (Mn/DOT Spec. 3149.2B2)	0.5	58	8.3	115	16.7	192	27.8	211	30.6	350	50
GRANULAR (Mn/DOT Spec. 3149.2B1)	NA	35	5.1	70	10.2	117	17.0	129	18.7	350	50

3.3.3 SUBBASE AND SUBGRADE PROPERTIES

The subbase and subgrade layer properties were characterized using the combined modulus of subgrade reaction (k_{comb}). As the granular subbase and subgrade support varies with season, mainly because of the subbase strength associated with the change in moisture content, different k_{comb} values were assigned for different seasons. The ACPA [18] static k_{comb} calculator was used to estimate the k_{comb} for different seasons. The thickness of the subbase layer and subgrade resilient modulus were the input for the estimation of k_{comb}. A screenshot of the webpage related to the ACPA static k_{comb} calculator is attached in the Appendix. Combined modulus of subgrade reaction values were calculated for each cells for various seasons. Later, k_{comb} was utilized in faulting prediction models discussed in Chapter 6.

CHAPTER 4: **JOINT FAULTING**

Joint faulting was measured on the test cells in different seasons between 2017 and 2019. Using a faultmeter, the joint faulting for each cell was measured routinely on ten joints (initially selected at random) at four different offsets from the centerline. The faulting measured at the ten transverse joints were averaged to determine the faulting magnitude for each cell. It should be noted that the pavement surface texture depth is usually around 0.04 inch (1 mm) on average; therefore, any faultmeter readings below $\pm$ 0.04 inch (1 mm) may not be indicating any notable faulting. A negligible faulting value (<1mm) may also indicate an undeployed joint. In an effort to investigate the deployment of transverse joints, MnDOT has tested all the transverse joints that showed less the 0.8 mm faulting with an ultrasonic tomography device (MIRA). As on October 2019, all but three transverse joints in the passing lane of Cell 606 (Joint Nos. 2541, 2543 and 2545) were found to be deployed. Each of the faulting plots in this chapter has a horizontal line at 1 mm (0.04 inch) faulting value indicating the trigger of faulting.

4.1 FAULTING VS AGE

Figure 8 shows the trend of faulting with respect to age for Cells 139 and 239. It is evident from the plot that faulting is less in Cell 239 (4-inch thick) as compared to Cell 139 (3-inch thick). As these two cells have same fiber dosage, support conditions, and traffic, it can be stated from the observed trend of data that one-inch extra concrete helped reducing faulting in Cell 239; however, the measured faulting for these two cells was around one 1 mm (0.04 inch), until May 2019, when faulting was measured last time.

Figure 9 shows that for thin unbonded concrete pavement overlays, faulting is affected by slab size. Cell 705 with larger slabs (driving lane 14 ft X 12 ft, passing lane 12 ft X 12 ft) experienced slightly less faulting as compared to Cell 805 with smaller slabs (driving lane 8 ft X 12 ft, passing lane 6 ft X 12 ft).

Figure 10 shows the faulting for the Cells 506 to 806 with respect to age, where fiber dosage was varied between the cells. It can be seen that the faulting decreased with the increase in fiber dosage or residual strength. The Cell 506, which did not have any fiber, experienced the largest magnitude of faulting among the four thin pavement cells; whereas, Cell 806, which had the maximum fiber dosage, experienced the lowest magnitude of faulting (3 times less than Cell 506).

Note that the magnitude of faulting with respect to age is much less in Cells 139 and 239 when compared with Cells 506 to 806, as seen in Figure 8 and Figure 10, respectively. The reason for this is that the Cell 506 to 806 are subjected to interstate traffic (I-94), whereas, Cells 139 and 239 are constructed in the low volume test track and carried far less traffic than other cells. Thus the comparison faulting with respect to ESALs would be more meaningful, as discussed in the next section.

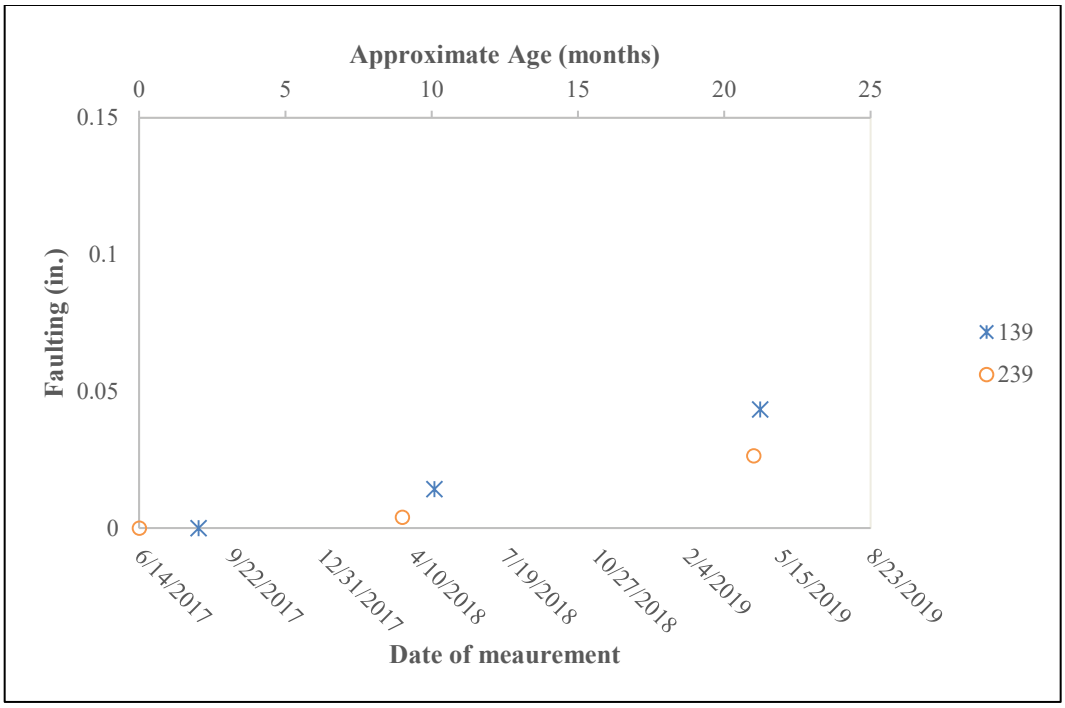

Figure 8: Faulting vs. Age for LVR test section (Cells 139 & 239)

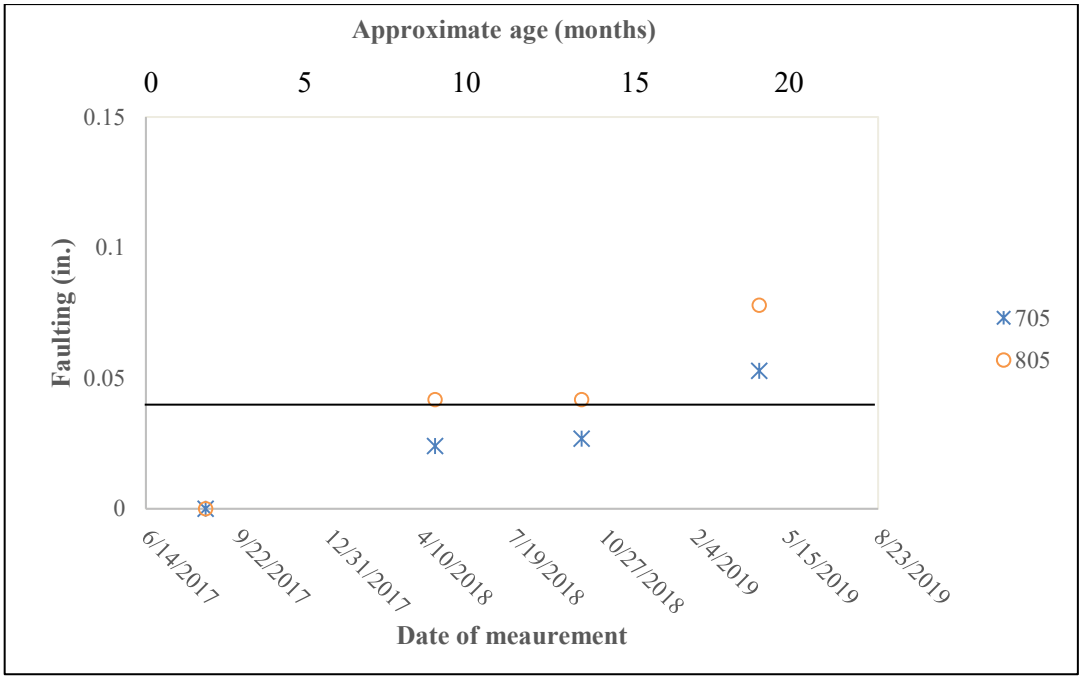

Figure 9: Faulting vs. Age for cells 705 & 805

Figure 10: Faulting vs. Age for cells 506,606,706 & 806

4.2 FAULTING VS TRAFFIC (ESAL)

Figure 11 shows the measured faulting for Cells 139 and 239 with respect to ESAL. Note that the estimated ESAL for a given number of axle load repetition is higher for the 3-inch thick cells than the 4-inch thick cell. When this slab thickness effect was considered in the ESAL calculation, it appears that the difference in the faulting values between the Cells 139 and 239 was not much, but as the total faulting accumulation was around 1 mm, any conclusion for the faulting for this two cells are not much relevant. Figure 12 shows that the larger sized slabs in Cell 705 developed less faulting as compared to the narrower sized slabs in Cell 805. Figure 13 shows the variation of faulting for Cells 506 to 806; this figure also shows the significant contribution of fibers in Cell 806. The sudden increase of the faulting at 1.8 million ESALs (during spring 2019) for all the thinner cells indicates a weakening of the joint conditions during the springtime when the underlying layers were relatively weak. There is no significant difference between the measured faulting values for Cell 606 and 706. This might be reasonable because even though the Cell 706 (5-inch) is one inch thinner than Cell 606 (6-inch), it contains 3 lb/cy more fibers than Cell 606; the residual strength of Cell 606 concrete is 124.16 psi compared to 156.4 psi for the Cell 706. Figure 14 compares the faulting values of all the thinner cells with respect to ESAL. This figure shows the far higher rate of faulting accumulation for the ultra-thin cells (Cells 139 and 239) compared to the thin cells (Cells 506 to 806).

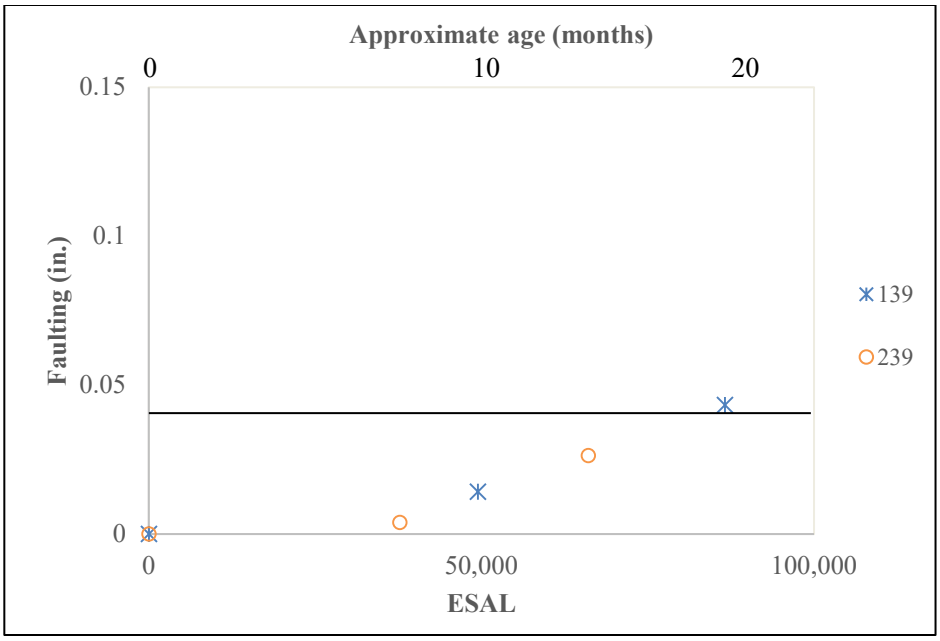

Figure 11: Faulting vs. ESALs for LVR test section (Cells 139 & 239)

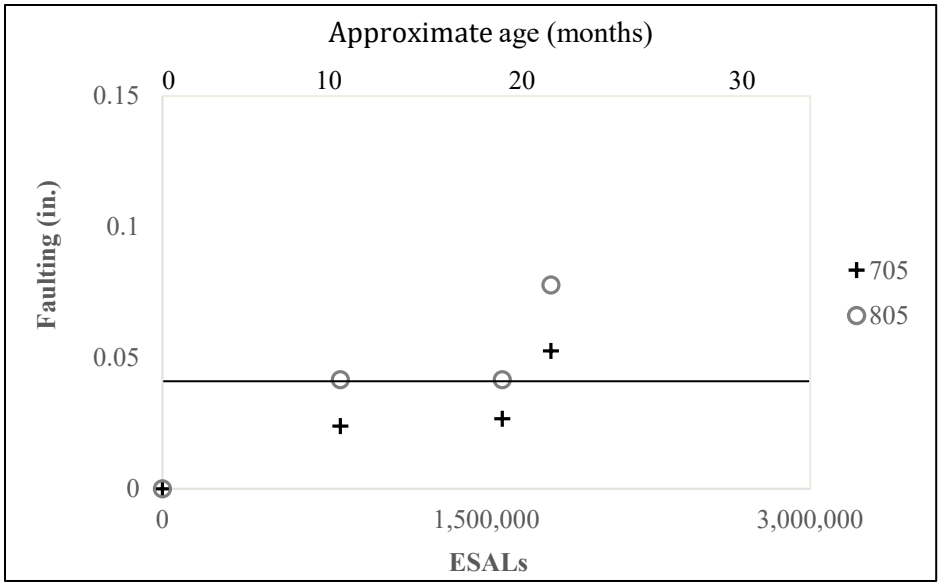

Figure 12: Faulting vs. ESALs for cells 705 & 805

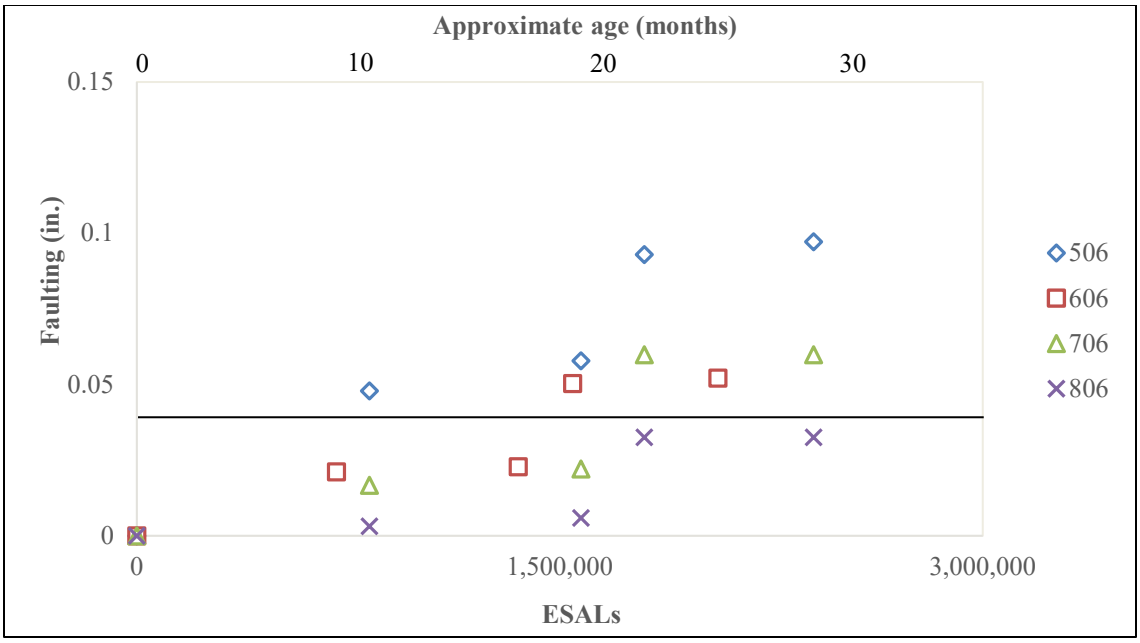

Figure 13: Faulting vs. ESALs for cells 506,606,706 & 806

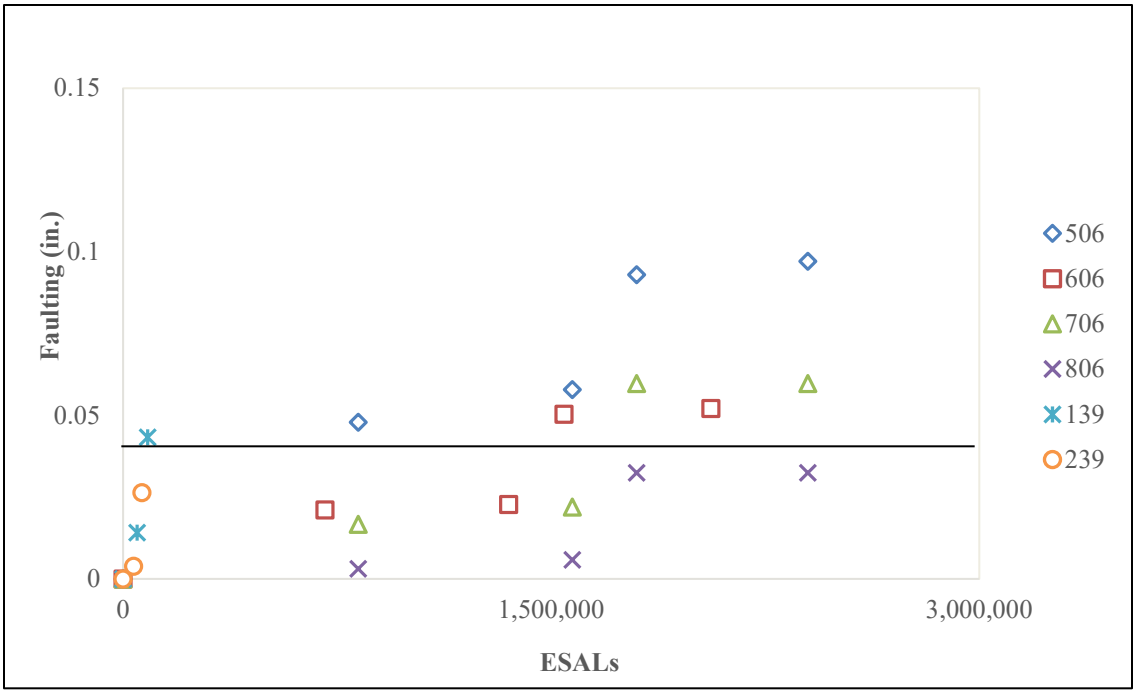

Figure 14: Comparison between low volume cells (139 and 239) and high-volume cells (506,606,706, and 806)

CHAPTER 5: **JOINT PERFORMANCE**

The joint load transfer behavior of all the eight cells was studied using the FWD test results collected for the driving lane. The tests were routinely conducted at selected joints in different times of the year between 2017 and 2019, except for Cell 139. Many slabs of Cell 139 experienced severe cracking and slab replacement [13], resulting in the cease of FWD testing in 2019. The FWD test results were used to determine the load transfer efficiency (LTE), slab displacement (D), differential displacement (DD), and to investigate the presence of voids underneath the slabs. LTE is the ratio of the displacement on the unloaded side of a joint to the loaded side of a joint, and expressed as a percentage; whereas, the absolute difference between the above mentioned two displacements are referred to as the differential displacement. The load side displacement in this study refers to the slab displacement (measured six inches away from the joint) under an FWD test. Higher slab displacements likely indicate weaker support conditions, or the loss of load transfer provided by aggregate interlock within the joint.

5.1 LOAD TRANSFER EFFICIENCY

Figure 15 through Figure 17 show the comparison of LTEs of different cells with respect to ESAL. Note that the x-axis of Cells 139 and 239 is different from other cells, because of the fewer number ESALs applied on Cells 139 and 239. As shown in Figure 15, LTEs for Cells 139 and 239, which was around 90% right after the construction, decreased with the increase in ESAL.

Figure 16 shows the change in LTE with ESAL for the two unbonded overlay Cells 705 and 805. These overlay cells were observed to have consistently lower LTE right from the construction period, as low as 30%. The exact reason is not clear at this stage, but it may be noted that the nonwoven geotextile fabric interlayer between the overlay and the original slab surface (constructed in the year 1993) might have a significant influence on the FWD results.

The LTE comparison among Cells 506 through 806 shows the influence of structural synthetic fibers. The LTE of the Cell 506 was approximately 10% lower than the three other cells right after the construction, which then significantly dropped and varied between 25 and 50%, depending on the season. On the other hand, the LTE trend in Cell 806 was very different. The LTE of this cell was 92% initially, which then decreased with ESAL, but at a slower rate than the other cells and still exhibiting 40% higher LTE than Cell 506 at the end of 1.8 million ESALs. Cells 606 had around 90% LTE initially and showed performance between Cells 506 and 806 until around 1 million ESALs, after which the LTE of this cell significantly dropped to 30%. Although the initial LTE of the Cell 706 was the same as Cell 806 (92%), it sharply dropped with the ESAL and then behaved like Cell 506.

The LTE observation in this study broadly indicates that the fibers contribute toward improvements in joint load transfer, but the LTE data of the Cells 606 and 706 (LTE is below 50% at 1 million ESALs), indicates a concern that a higher fiber dosage may be required for

achieving long term benefits from fibers in mitigating joint faulting, at least for the type of synthetic fiber that was used in this study. However, it shall also be noted that the accelerated nature of loading (one million ESALs per year) applied on the thin test cells in the current study, which is not likely to occur in typical low volume roads, might have accelerated the damage to the fibers at a faster rate than that which would occur in real applications. The loss of LTE benefit from the fibers (stretching, breaking or being pull out of the concrete) is also caused by the natural shrinkage of the concrete panels and the opening of joints in wintertime temperatures.

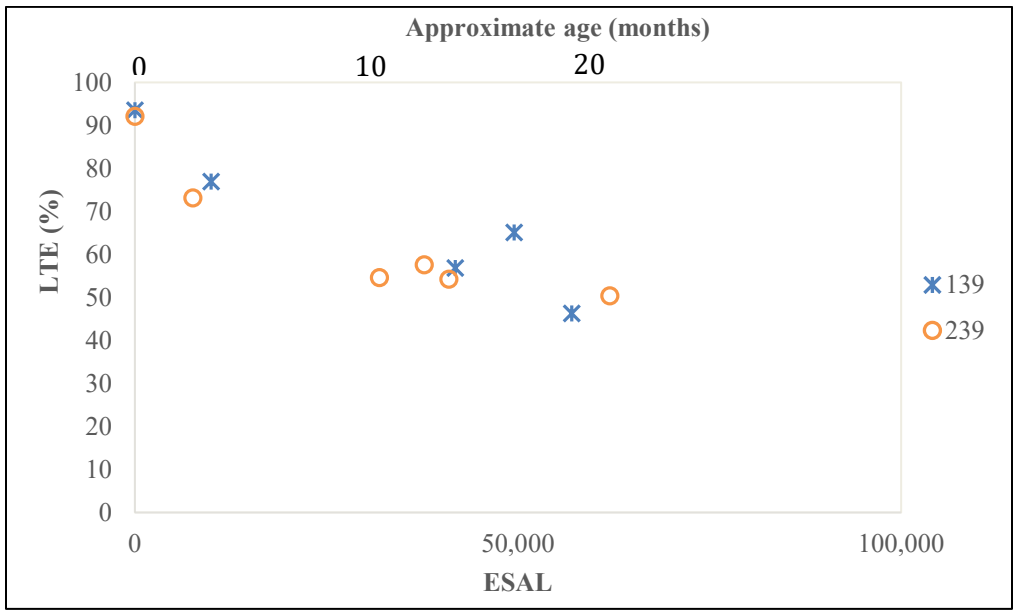

Figure 15: LTE vs ESALs for Cells 139 and 239

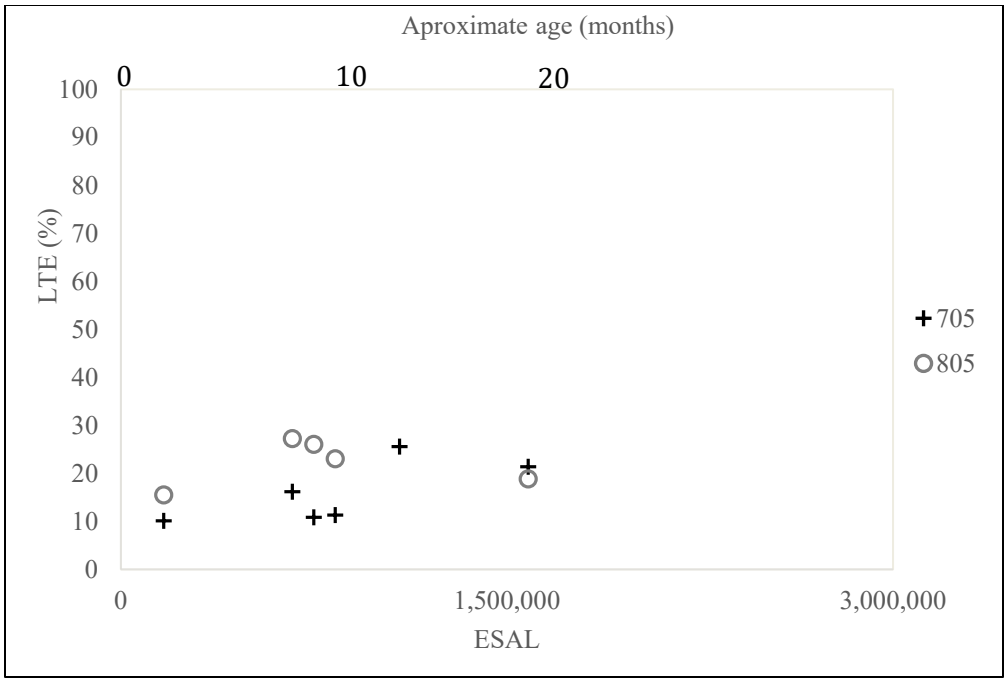

Figure 16: LTE vs. ESALs for Cells 705 and 805

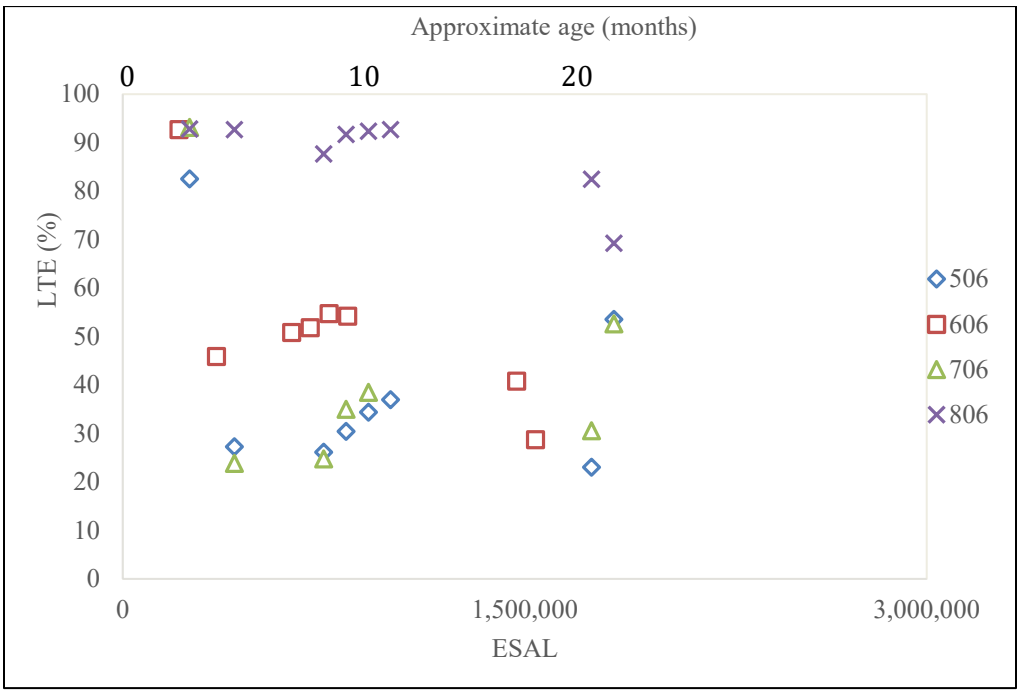

Figure 17: LTE vs. ESALs for Cells 506, 606, 706 and 806

5.2 DIFFERENTIAL DISPLACEMENT

Figure 18 through Figure 20 show the differential displacement for the Cells 139-239, 705-805, and 506-806, respectively. An increase in the differential displacement means higher relative movement between the slabs or weaker joint conditions. The differential displacement for Cell 139 was comparable with Cell 239 until about 50,000 ESALs, but then suddenly increased, indicating a significant deterioration at the transverse joints. Cell 705 and 805 had very close differential displacement values with a maximum of 30 mils for Cell 705. The differential displacement values for Cells 506 through 806 were lower than that of the Cells 139 and 239 for a given ESAL. Cell 506 exhibited the highest differential displacement, and Cell 806 had the lowest among the thin concrete overlays. Even though the LTE of Cells 706 and 506 were similar for a significant length of service (before 1.8 million ESALs), the differential displacement of Cell 706 was less than that of the Cell 506.

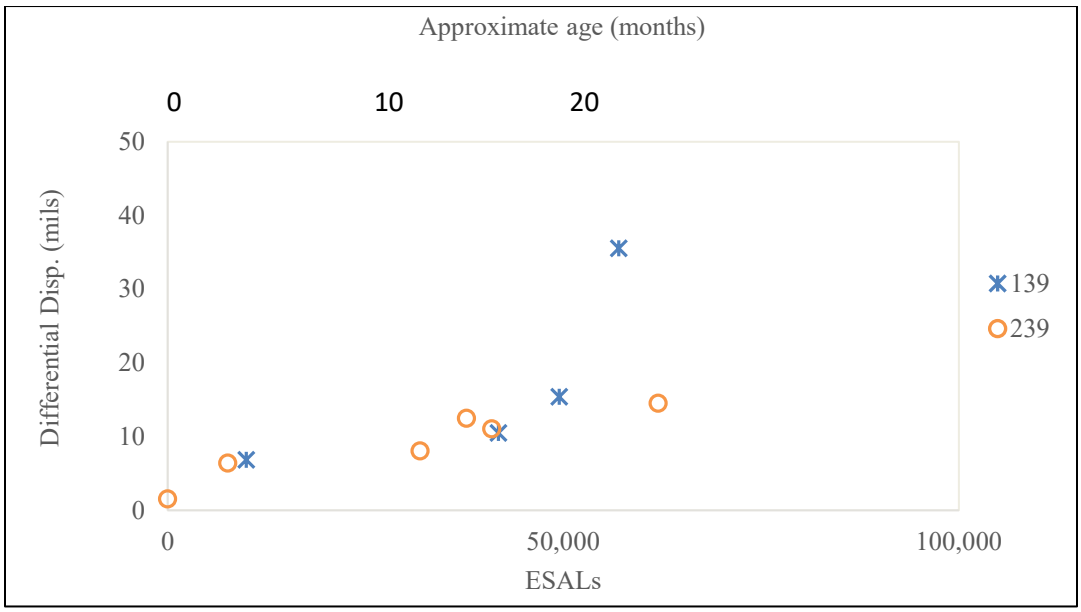

Figure 18: Differential displacement vs ESALs for Cells 139 and 239

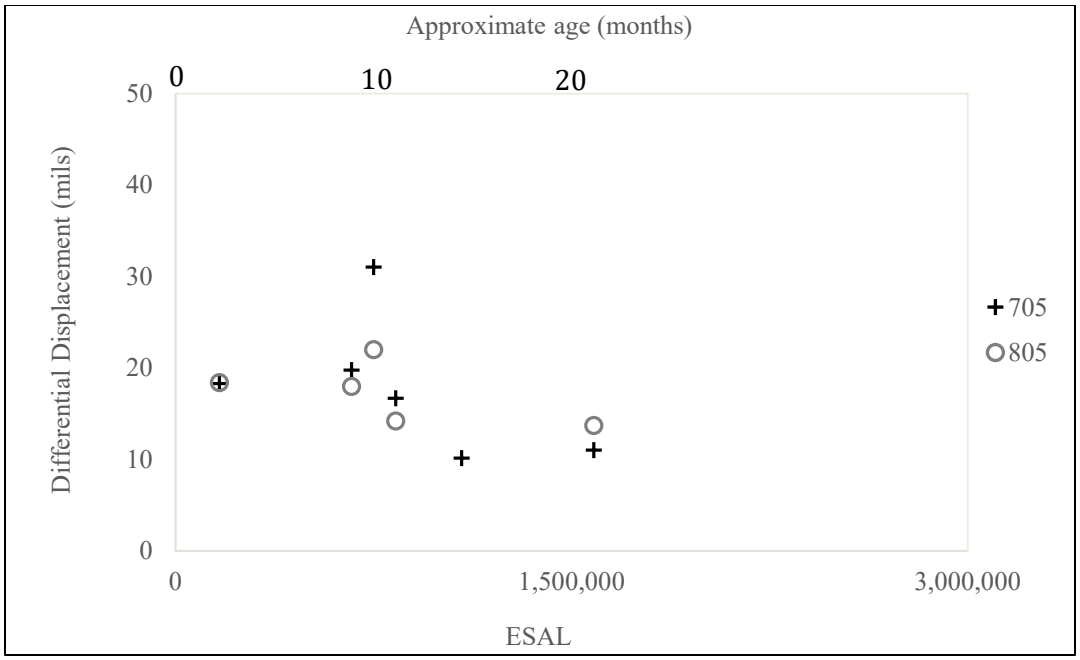

Figure 19: Differential displacement vs. ESALs for Cells 705 and 805

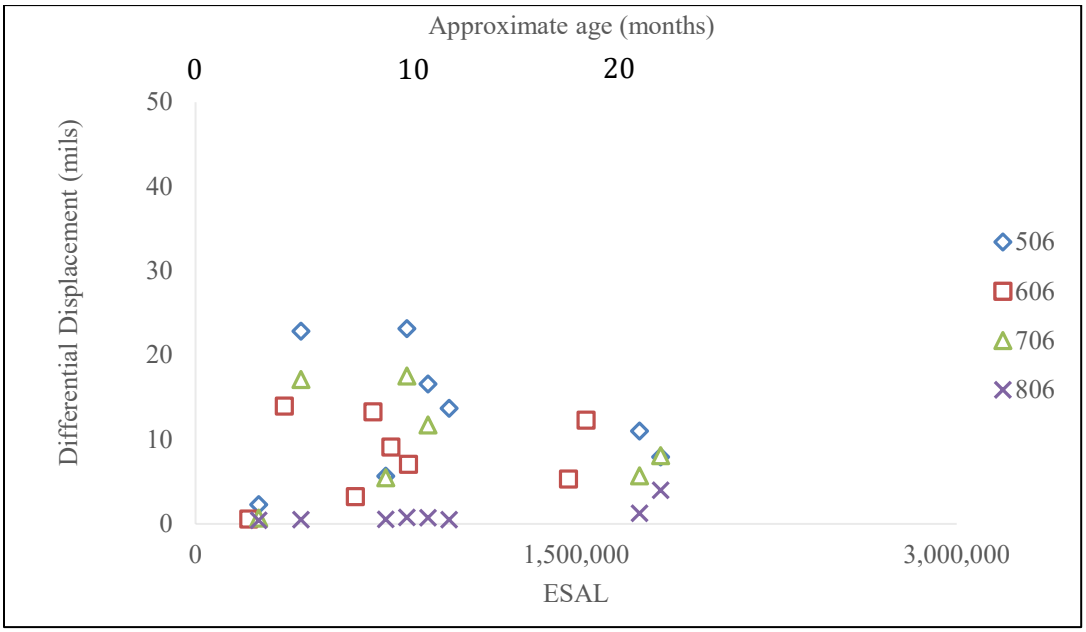

Figure 20: Differential displacement vs. ESALs for Cells 506, 606, 706 and 806

5.3 SLAB DISPLACEMENT

Figure 21 through Figure 23 show the slab displacement trend for Cells 139-239, 705-805, and 506-806, respectively. Cell 139 had very high slab displacements as the ESAL increased,

especially after 50,000 ESALs, as compared to its 4-inch-thick counterpart Cell 239. Slab displacement of Cell 239 did not change too much with ESALs.

Cells 705 and 805 had followed similar trends, except for one test date at 75,000 ESALs. These two cells always showed lower joint load performance, as indicated by the poor LTE (Figure 16) and differential displacement (Figure 19) results discussed above. It can be seen that the difference between the differential displacement (Figure 19) and slab displacement (Figure 22) values for a given test is much smaller; in other words, the unloaded slabs did not deflect much (less responsive). The reason for this is the presence of the compressible geofabric layer at the interface and the considerable strong base. The FWD load (9,000 lb) at the loaded side slab compresses the geofabric layer resulting in significantly higher deflection at the loaded side compared to the unloaded side slab. The deflection consumed by the strong base is assumed to be minimal on either side of the joint. The above assumption was verified with the help of the light weight deflectometer (LWD) test. In summer 2020, a couple of slabs of Cell 805 were replaced because of severe fatigue cracking. When the broken slabs were lifted, the LWD test was conducted on the exposed base at five different locations, initially on top of the geofabric layer and then on the concrete base layer (without geofabric). The LWD load was 22 lb (10 kg), and the diameter of the load plate was 8 in (200 mm). Figure 24 compares the LWD measured deflections. It can be seen that the deflection on the base with geofabric was 5 to 15 times more than the deflection of the base alone. The average deflection on the base with and without geofabric were approximately 18 and 2, respectively. It may be stated that a similar difference may not be achieved when 9,000 lb load is applied on top of the slab (not on the base), but it is anticipated that a considerable amount of deflection will be resulted in because of the compression of the geofabric. The abovementioned finding also brings up the question of whether the FWD measured LTE is an accurate representation of the joint performance for the unbonded overlays when there is a compressible layer at the interface. The other concern is the relatively higher differential displacement at the transverse joints of such overlays, which can abrade the texture of the deployed joints or crack face, decreasing the aggregate interlock and damaging fibers at a faster rate. This may not aggravate the faulting because of the presence of the geofabric layer, but likely to keep the load-induced stresses high on the loaded slabs, resulting in fatigue cracks.

The load side displacements for the thin pavement cells (Cells 506-806) were lower relative to ultra-thin Cells 139 and 239. Cell 506 had higher load side displacement than the three other thin pavement cells, indicating the contribution of fibers in transferring loads across joints in FRC. Cell 806 had negligible slab displacement compared to the other three cells.

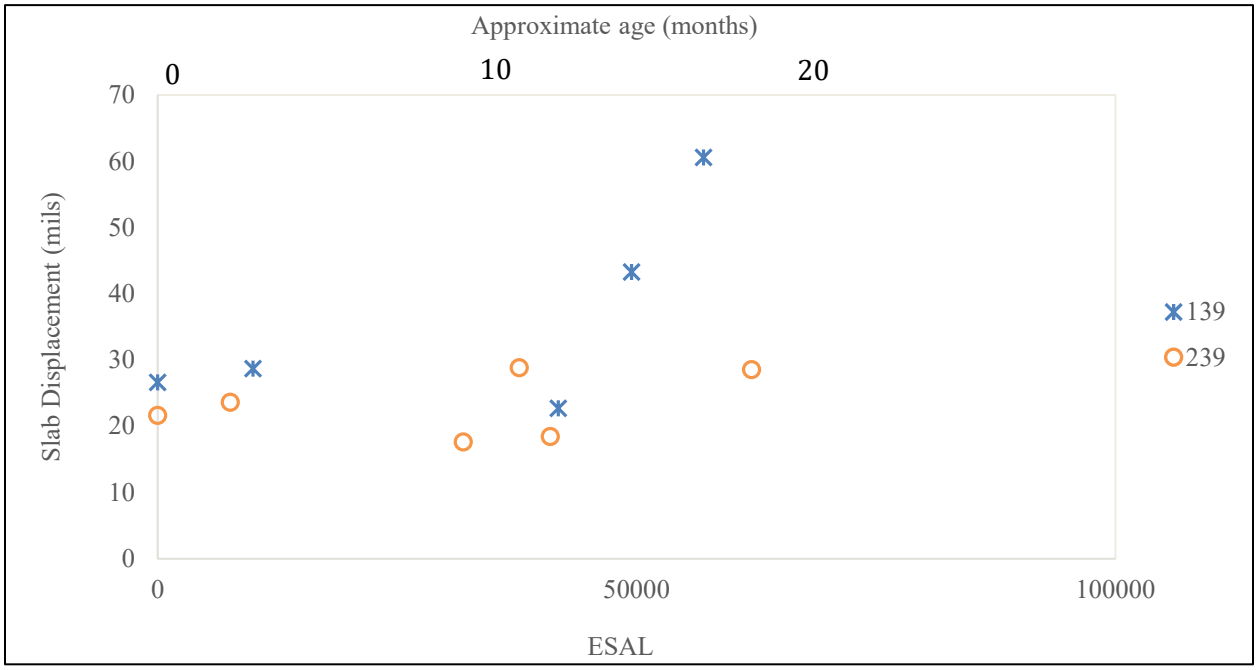

Figure 21: Slab displacement vs. ESALs for Cells 139 and 239

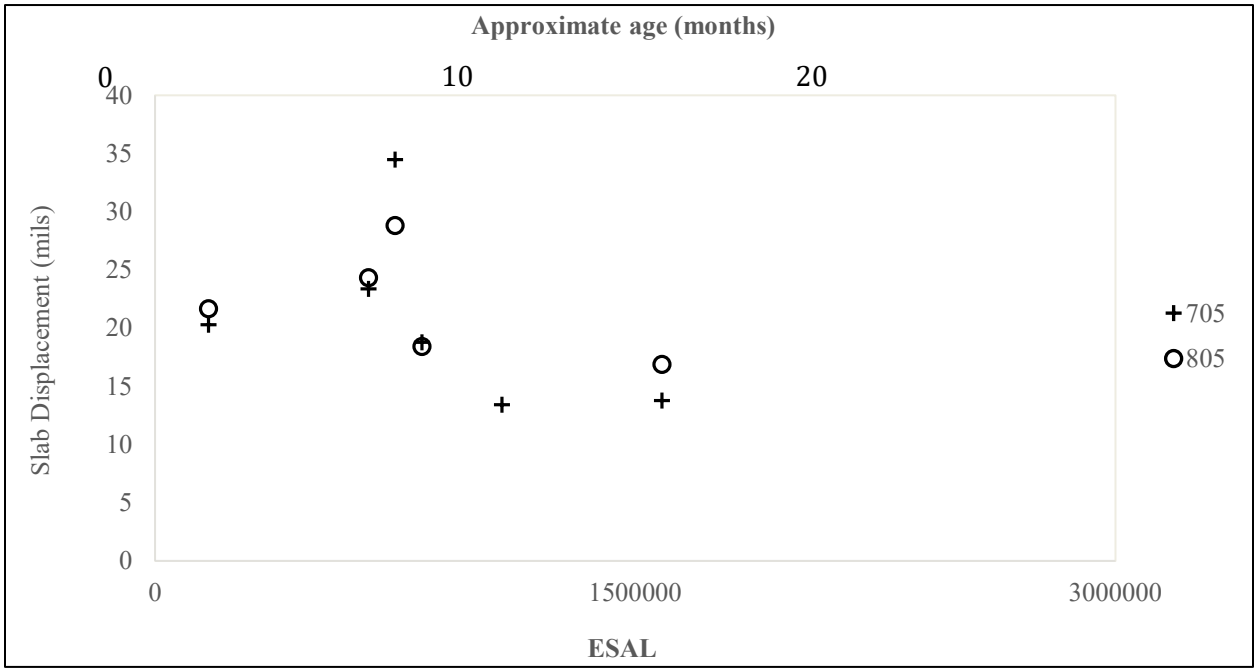

Figure 22:Slab displacement vs. ESALs for Cells 705 and 805

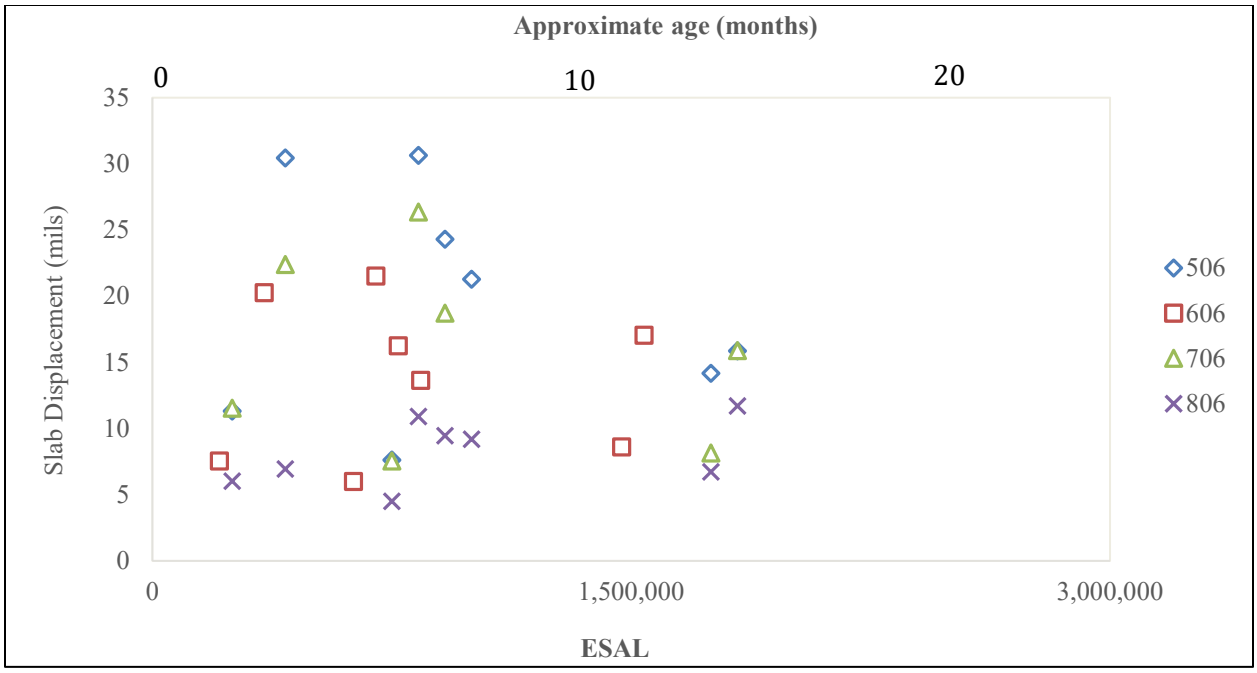

Figure 23: Slab displacement vs ESALs for Cells 506, 606, 706 and 806

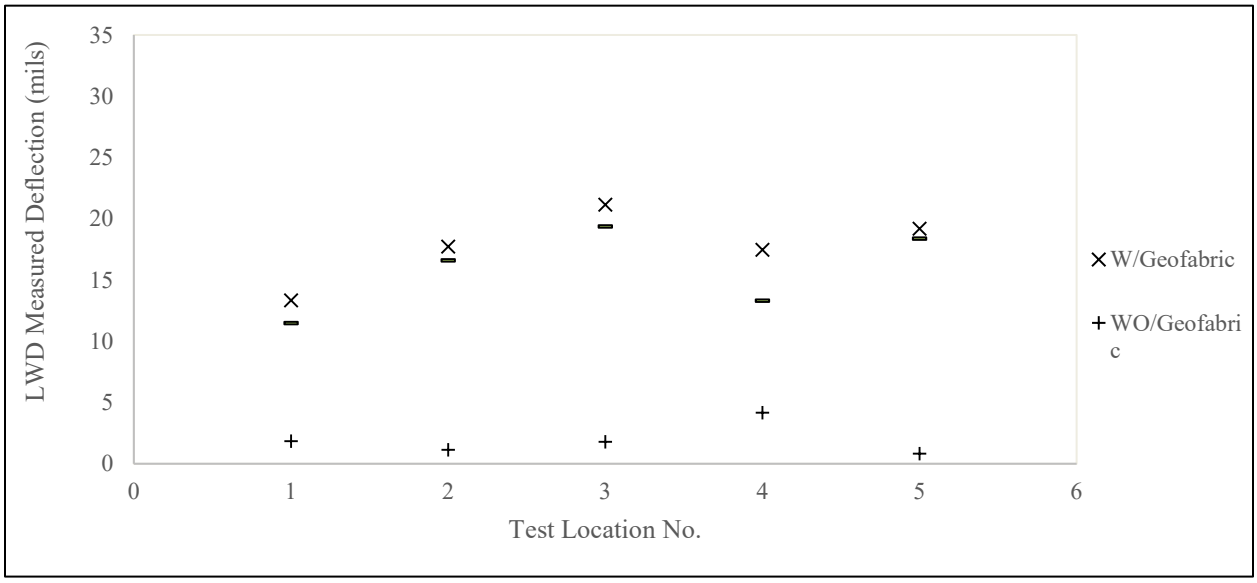

Figure 24: Deflections measured by LWD test on the underlying concrete base layer

5.4 LTE VS PAVEMENT SURFACE TEMPERATURE

The load transfer behavior of fiber reinforced concrete is dictated by the aggregate interlock and dowel action of the fibers. Both of these parameters are influenced by crack width variation, which is a function of the temperature and the relative humidity of the slabs to a certain extent.

In the summertime, when the temperature remains high, the crack width closes, and the LTE increases. The exact opposite occurs in winter, but the frozen base and subbase then play a supporting role in transferring the wheel loads. During the spring-thaw season, the joint width still remains wide, in which case the weak support conditions of the granular base can result in low LTE.

Figure 25 to Figure 27 shows that the LTE measured for almost all the cells increases when the pavement surface temperature increases. Figure 25 shows that Cell 139 and 239 have almost similar characteristic when it comes to variation of LTE with pavement surface temperature. Cell 705 and 805 as shown in Figure 26 had the least reported LTE of all the eight cells, but they did not vary much with the temperature. It was observed that the variation of LTE with temperature was more sensitive in 705 compared to 805 (narrower slabs).

However, the most interesting observation is the influence of fibers on the LTE vs. temperature relationship. Figure 27 shows Cell 806 experienced the least change in LTE with respect to temperature, indicating the contribution of fibers toward increasing load transfer through dowel action in the wider cracks at low temperatures. The fibers are also likely serving to increase the aggregate interlock by keeping the joint widths tight. LTE variation was more pronounced for the Cell 506 (plain concrete). The slope of the LTE vs. temperature line for Cell 706 is also sharp, which indicates the greater influence of the temperature. The exact reason for Cell 706's low joint performance is not known; however, the data indicate that the joints considered for the FWD test probably experienced damages because of the higher load side displacement, differential displacement, and presence of voids underneath at very early age. Note that even though the design RSR for this cell was 30%, the beam samples prepared at the field only resulted in 23% RSR, which is close to Cell 506's RSR.

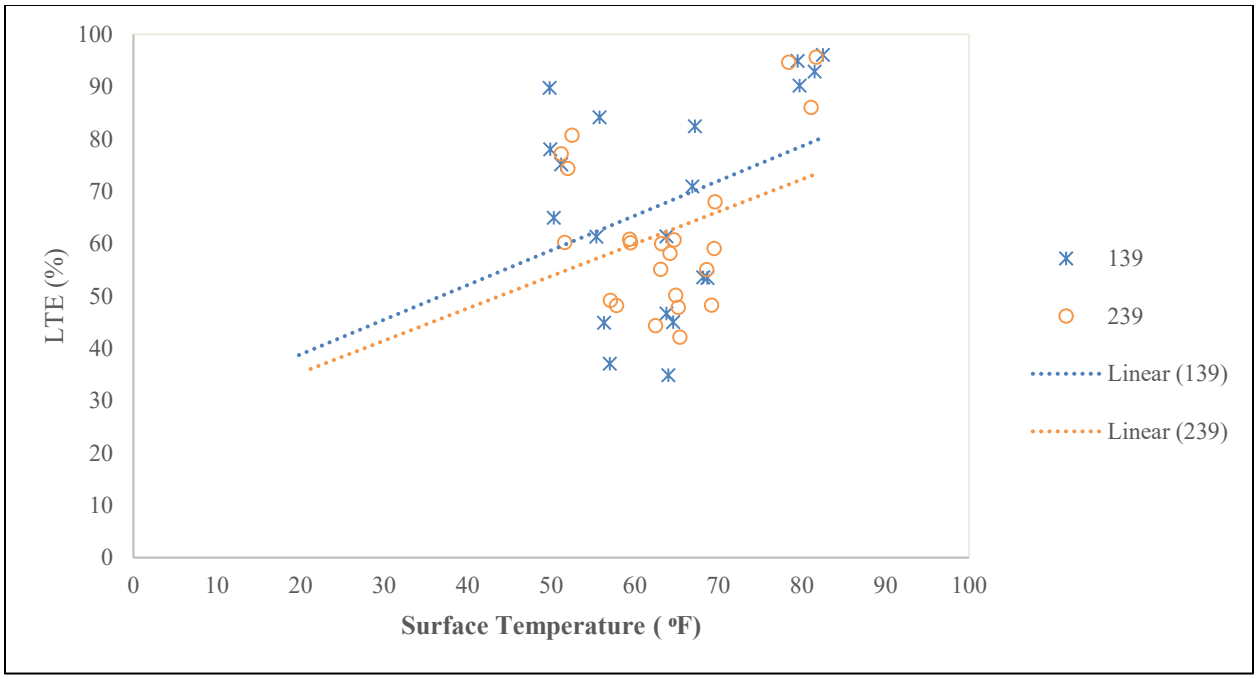

Figure 25: LTE vs. Pavement surface temperature for Cells 139 and 239

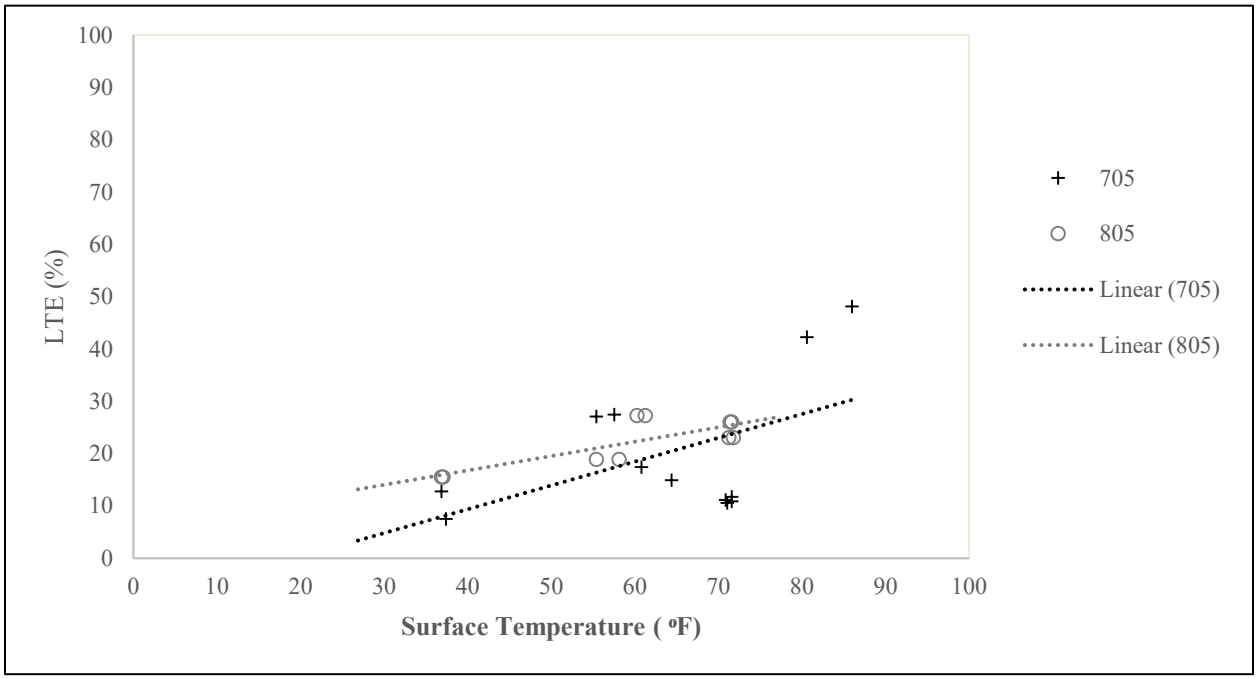

Figure 26: LTE vs. Pavement surface temperature for Cells 705 and 805

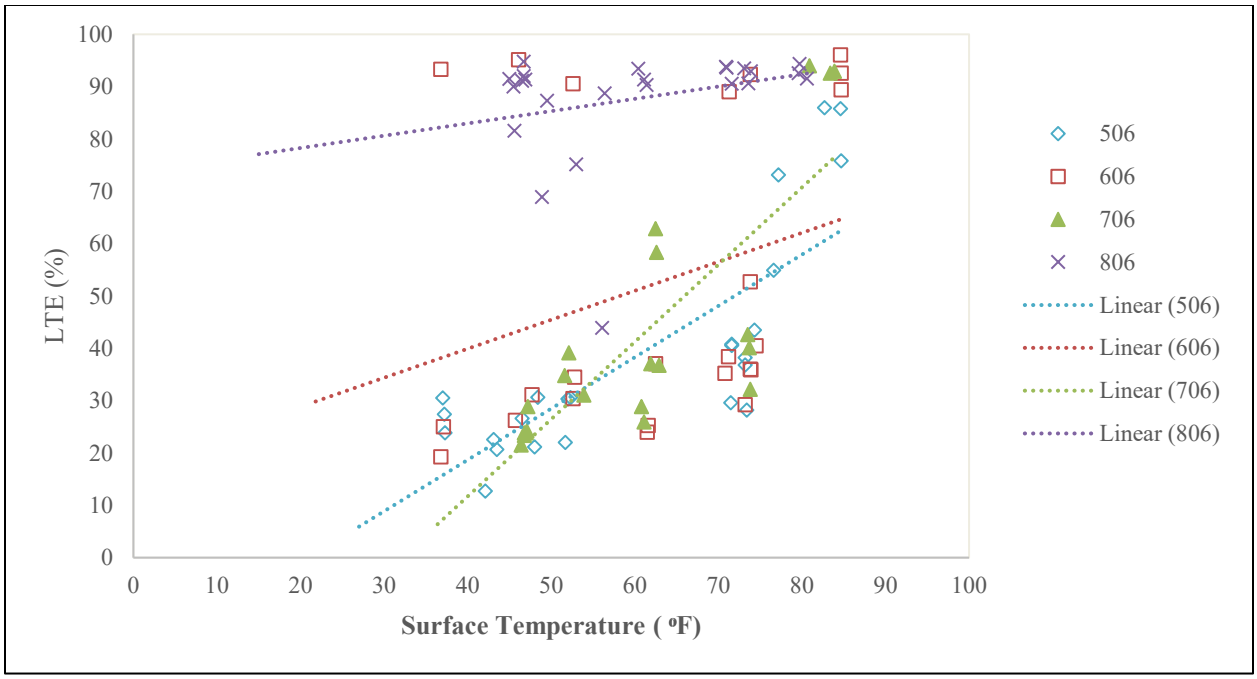

Figure 27: LTE vs. Pavement surface temperature for Cells 506, 606, 706 and 806

5.5 VOID DETECTION AND VOID INDEX CONCEPT

Crovetti and Darter (1985) [19] proposed a method to investigate the presence of voids underneath concrete pavement slabs using FWD test results. As shown in Figure 26, FWD-measured corner deflections are plotted against the applied loads in this procedure. In such a plot, if the intercept of a deflection line (at zero load) is two mils or below, then it is assumed that the chance of void presence is low. A similar concept was adopted in the current study to identify the presence of voids under the slabs and to understand the influence of the fiber, if any. One exception in the current study was the use of slab deflections along the wheel path at the transverse joint, instead of corner deflections. Also, it may be noted that the deflection data collected at the leave slab with the load on the leave slab was used for the void detection analysis, because of the probability of more void presence under the leave slabs. Figure 27 (a) and (b) compare the deflection vs. FWD applied load at one particular slab in Cell 506 (plain concrete cell) and Cell 806 (highest fiber dosage). Deflections were measured at different seasons for both the cells. While it appears that the deflection intercept determined for the spring-thaw times were relatively higher than the other seasons for both the cells, Cell 506 had higher values than the Cell 806. Figure 28 summarizes the deflection intercept for all the ultra-thin and thin pavement cells for various slab and test dates. Cells 705 and 805 were not considered for this analysis as they are overlays and have geofabric layer underneath the slabs.

The deflection intercept values calculated for different seasons for all the cells were used to determine a factor, referred to as 'void index (VI),' to quantify the influence of fibers to the void

accumulation underneath the slab, especially at the wheelpath-transverse joint intersection. This void index depends on the amount of FWD detected voids present under slabs, with 5 being the best condition with no voids, and 0 being the worst condition with excessive voids underneath the slab. Table 7 presents the proposed scale of VI for different ranges of deflection-intercepts. This scale was used to determine the VI for all the cells at different seasons using their respective deflection intercept, as presented in Table 7. It appears that Cell 139 shows a good trend with VI, decreasing from 3 to 1 in one year; Cell 239 had better VI values than Cell 139, and it did not decrease much with age. The comparison of VI values between Cell 806 and other cells indicates that the higher fibers in Cell 806 were able to significantly protect this cell from void (FWD detected) formation underneath the slab. The results for the Cells 506, 606 and 706 indicate that these cells seem to have significant FWD detected voids underneath their slabs, and the recent declines in LTE and increases in the faulting agree to this finding.

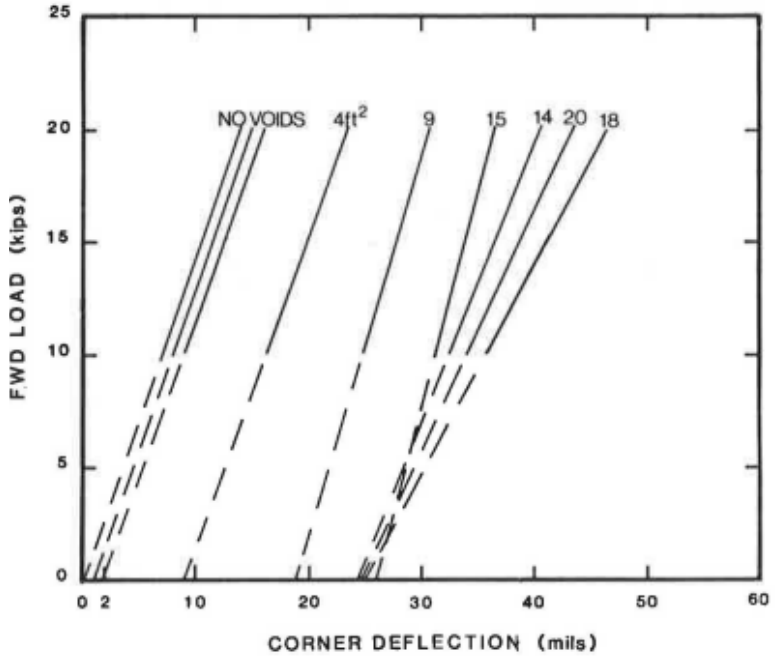

Figure 28: Use of FWD test data conducted at different load level to identify possible presence of voids (Crovetti and Darter, 1985)

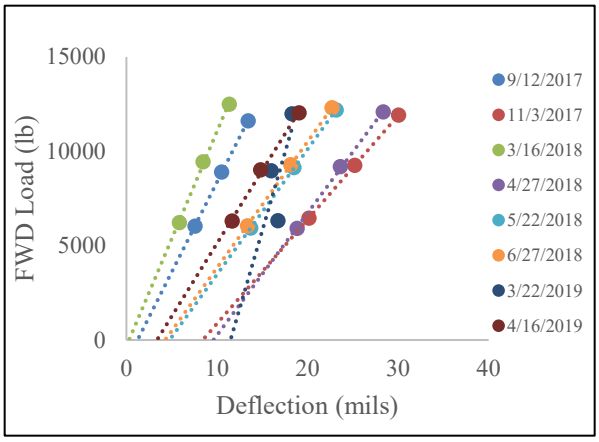

(a)

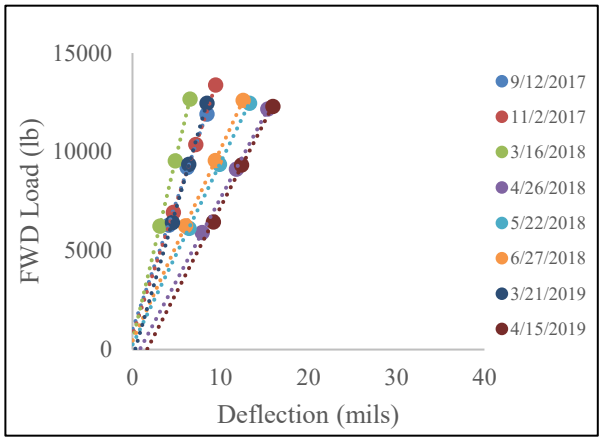

(b)

Figure 29: Deflection vs FWD load for (a) Cell 506 (b) Cell 806

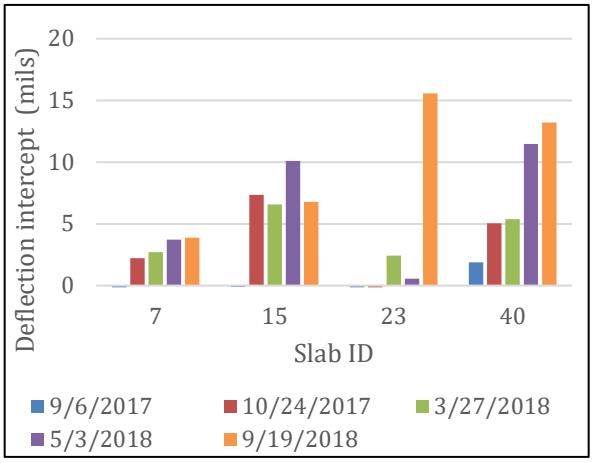

(a)

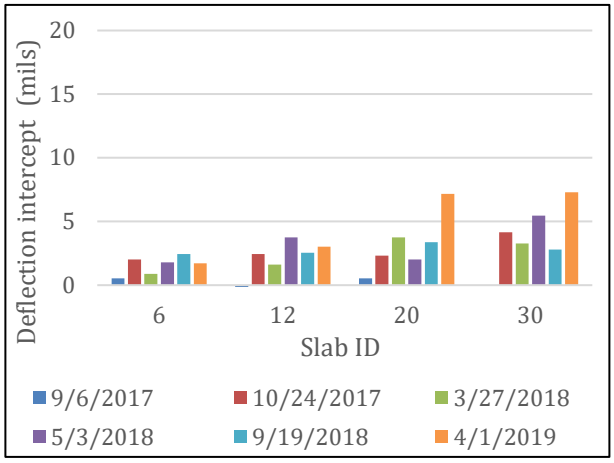

(b)

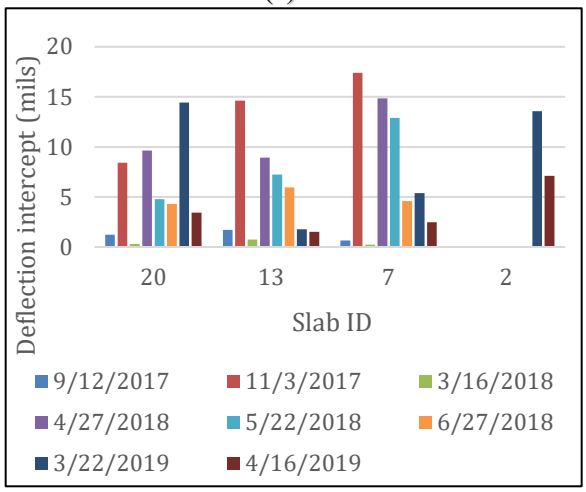

(c)

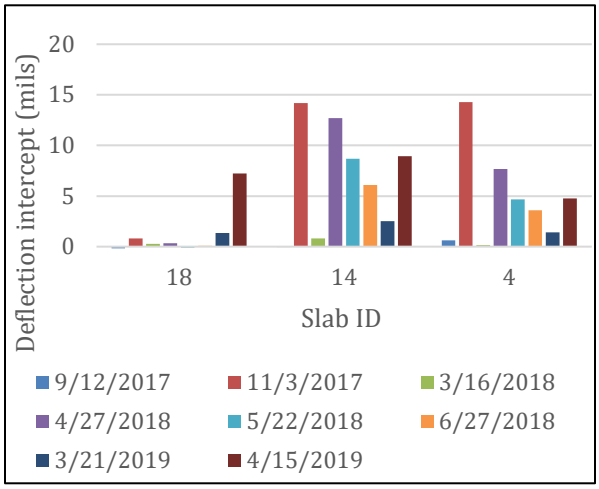

(d)

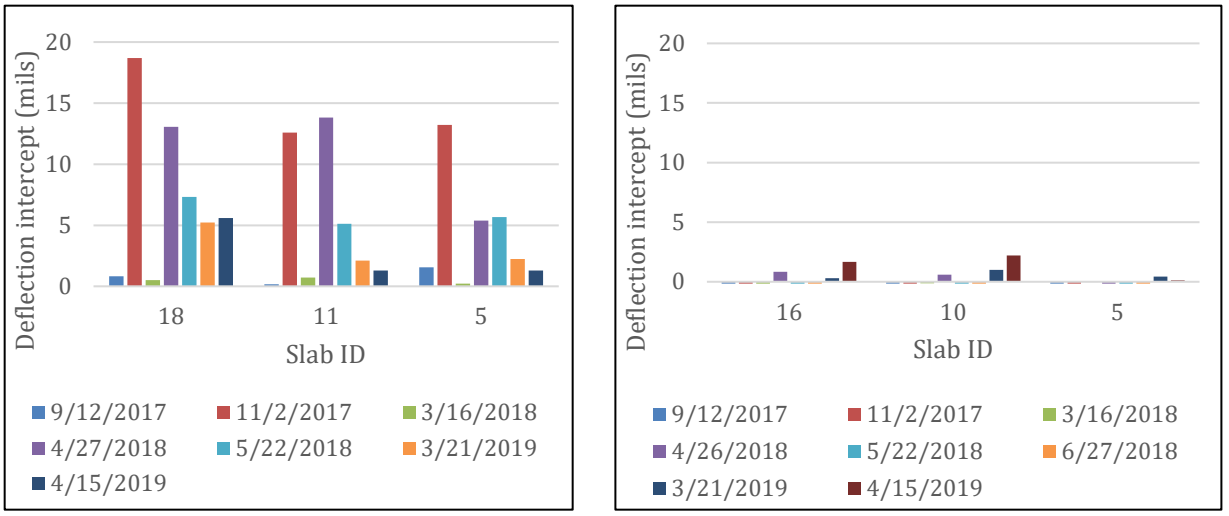

(e) (f)

Figure 30: Deflection values under variable FWD load stresses for NRRA test Cells (a) 139 (b) 239 (c) 506 (d) 606 (e) 706 and (f) 806

Table 7 presents the VI values for available deflection recorded. FRC test cells under consideration were then assigned with certain VI values as given in the following Table 8. These values were later used as input parameters while developing statistical faulting prediction models.

Table 7: Scale of the proposed void index.

VI	Voids possibility	Deflection
5	Nil	<2 mils
4	Very less	2-4 mils
3	Less	4-8 mils
2	Moderate	8-12 mils
1	Severe	12-16 mils
0	Very Severe	<16 mils

Table 8: Void index values for different cells at different seasons

	Void Index (VI) values				
Cell	Fall 2017	Spring 2018	Summer 2018	Fall 2018	Spring 2019
139	3	2	-	1	-
239	4	3	-	3	3
506	0	0	0	-	0
606	1	1	1	-	1
706	0	0	-	-	0
806	5	5	5	-	4

CHAPTER 6: FAULTING MODEL DEVELOPMENT

The data presented in the previous section verified that structural synthetic fibers can influence the joint behavior of ultra-thin and thin concrete pavements, including some contribution toward mitigating joint faulting. The mechanistic-empirical design of FRC thin pavements thus should consider the contribution of structural fibers in faulting mitigation. This study provided an opportunity to quantify the contribution of synthetic structural fibers. Faulting of a concrete pavement depends on many parameters. The National Cooperative Highway Research Program (NCHRP) final report for Transverse Joint Faulting [2] summarized various pavement variables that were considered in various faulting predicting models for conventional concrete pavements. It appears that ESAL, drainage coefficient, modulus of subgrade reaction, slab thickness, joint spacing, and shoulder types are some influential variables for faulting, with fiber properties now a logical addition to such parameters. This study introduces two faulting prediction models using the data discussed in the previous section. Cells 705 and 805 have the same fiber dosage, and their design is different than the rest; therefore, these two cells have not been considered in the modeling work, the primary focus of which is characterizing the fibers' contribution in joint faulting mitigation.

6.1 MODEL A

This model considered the influence of ESAL, slab thickness, and fiber property (residual strength of concrete) on faulting development. The general form of Model A is shown in Equation (5), which was developed using non-linear regression analysis. This model did not include the effect of the base thickness or any other base layer material properties.

$$FAULT = ESAL^{0.54} * (A + B * h + C * RS) \quad (5)$$

Where,

FAULT = Predicted faulting, inch.

ESAL = Equivalent number of 18-kip standard axles

h = Slab thickness, in.

RS = Residual strength of concrete, psi.

A, B, and C are parametric constants with values as 0.0000656, -0.0000063, and -0.0000000952, respectively. The R^2 and SSE for this model are 0.83 and 0.0035 inch.

Figure 29 shows the predicted and measured faulting values for ultra-thin and thin pavement cells (Cells 139-239 and 506-806) that were constructed with varying fiber dosages. Although the Model A was not very accurate for the Cells 139 and 239, the predicted and measured faulting values for Cells 506 through 806 show considerable matching between themselves. The inaccuracy of the model for the Cells 139 and 239 is because of the avoidance of the base layer properties in the model; it may be noted that the base for the Cell 139 and 239 was weaker compared to that for the Cells 506-806. Model A also could not detect the sudden jump of the faulting values during the spring season, when the base and subgrade remains the

weakest. Figure 30 shows that Model A could predict the faulting with an $R^2 = 0.83$. The Sum of Squared Errors (SSE) for this model was 0.0035 inches.

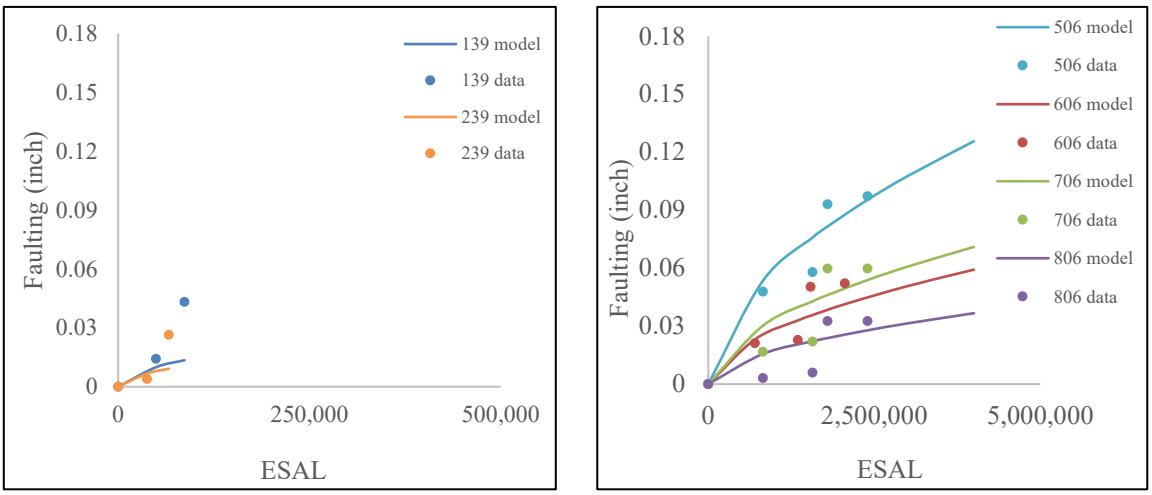

(a) (b)

Figure 31: Comparison of the measured faulting and Model A predicted faulting for (a) Cells 139 and 239, (b) Cells 506, 606, 706 and 806

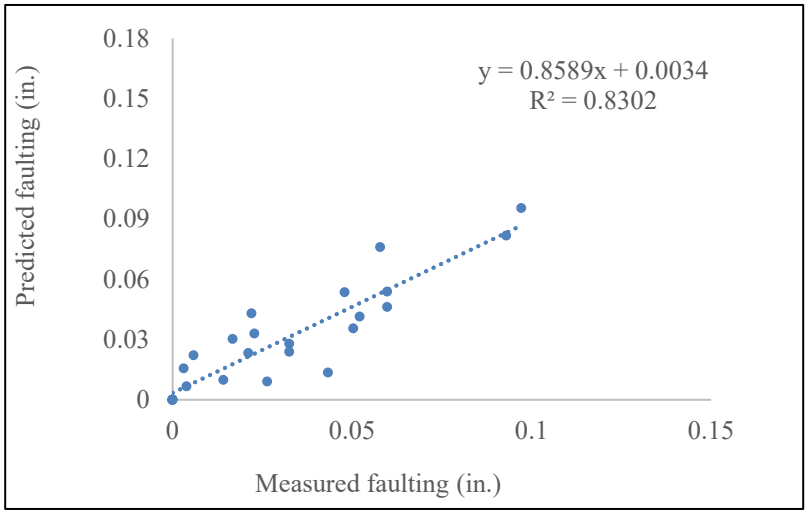

Figure 32: Predictability of Model A

6.2 MODEL B

Model B includes the effect of the underlying base layer and subgrade in terms of combined modulus of subgrade reaction (k_{comb}) and base layer thickness. As the granular base and subgrade support varies with season, mainly because of the base strength associated with the change in moisture content, different k_{comb} values were assigned for different seasons. Faulting data for Cells 139 and 239 was available for summer

and late spring, while data for Cells 506 through 806 was available for late spring, summer, and fall for different years. Therefore, two k_{comb} values were calculated for Cells 139 and 239, and three k_{comb} values for the other cells. Also, the materials and thickness of the base of the ultra-thin and thin pavement sections, which were not the same, influenced the values of k_{comb}. The late spring and summer k_{comb} for ultra-thin cells were 267 and 491 psi/in; whereas, the k_{comb} for thin pavement cells were 304, 551 and 637 psi/in for late spring, summer, fall, respectively. The seasonal subgrade resilient modulus and base modulus for determining the k_{comb} were collected from the Pavement Manual [15]. This model also considered the void index defined in the previous section. Figure 31 shows the comparison of field data and Model B predicted data for (a) Cells 139 and 239 and (b) Cells 506 to 806. The model is given in Equation (6).

$$FAULT = ESAL^{0.54} * (A + B * h + C * RS + D * k_{comb} + E * h_{base} + F * VI + G * ESAL^{0.1}) \quad (6)$$

Where,

k_{comb} = Combined modulus of subgrade reaction, psi/in.

h_{base} = Thickness of base layer, in.

VI = Void index

A, B, C, D, E, F and G are parametric constants; A= 0.000104868, B= -0.000000858136, C = -0.0000000942067, D= -0.000000106092, E= -0.00001745, F= -0.0000001313, G= 0.00004218. Other variables have been previously defined.

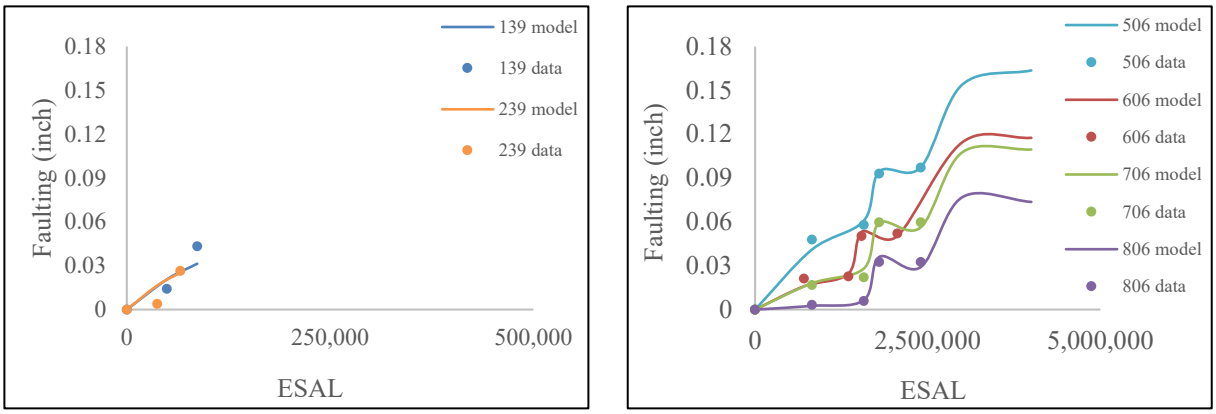

(a) (b)

Figure 33: Comparison of the measured faulting and Model B predicted faulting for (a) Cells 139 and 239 (b) Cells 506, 606, 706 and 806

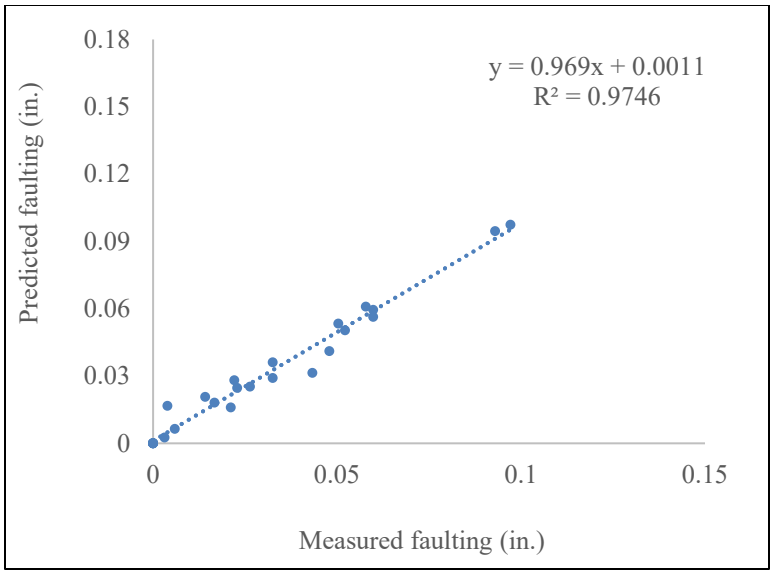

Figure 34: Predictability of Model B

Figure 32 shows that the Model B, in general, could predict the faulting with an $R^2 = 0.97$ and SSE = 0.000522 inch. Unlike Model A, this model could predict the jump in the faulting magnitude during the spring seasons. Inclusion of the base layer thickness (h_{base}), variation in the combined modulus of subgrade reaction (k_{comb}) and void index (VI) was helpful in modeling the sudden shift of the faulting in the spring season.

CHAPTER 7: **CONCLUSIONS**

Thin concrete overlays or pavements with fiber reinforced concrete on low volume roads may last longer and yield more economic benefits compared to many other alternatives. While structural fibers have been used in thin concrete overlays since many decades in the U.S., their benefits in terms of faulting mitigation are not properly studied and thereby not considered in the currently available mechanistic-empirical design procedures. Under the scope of this task, two ultra-thin (3 and 4 inches thick) and four thin (5 and 6 inches thick) pavement test cells, in addition to two thin (5 inches thick) unbonded concrete overlays, were constructed at MnROAD with the objective to quantify the benefits of structural synthetic fibers in mitigating the typical distresses that may occur. In this task report, the influence of the structural fibers on the joint performance behaviors and faulting trends of these cells were discussed during their service period between 2017 (when they were constructed) and 2019.

The contribution of the fibers was apparent in the faulting results. Cell 506, which was constructed with plain concrete, experienced considerably higher faulting than the three FRC Cells (606 through 806). The faulting increment rate with respect to ESAL was also higher for Cell 506 than the other cells.

The joint performance behavior evaluated by the falling weight deflectometer (FWD) revealed that fibers positively influence the load transfer efficiency (LTE), or other joint performance parameters for thin concrete pavements, depending on the fiber dosage. Between the four thin pavement cells (506 through 806) in which the fiber dosage was varied, the LTE of the Cell 806 (highest fiber dosage, 11.66 lb/cy) was significantly greater than the Cell 506 (no fiber). The contribution of the fibers in joint performance results of two other cells (606 and 706) was less, or not significant. However, the accelerated loading nature of the test section could have had an effect on the fiber performance. Another significant observation was the consistent low joint performance of the unbonded concrete overlays constructed with the compressible geofabric at the interface. Fibers' contribution could not be recognized on the two unbonded concrete cells (705 and 805). FWD test results compounded with the LWD test results indicated that the geofabric layer could result in higher differential deflection at the transverse joints, leading to faster abrasion of the aggregate interlock and damage to the fibers.

FWD test results also found that the synthetic structural fibers can decrease the influence of pavement temperature (seasonal temperature) change on the load transfer efficiency. The results presented in this study showed that with increased residual strength (or fiber dosage), the transverse joints communicate better, resulting in higher load transfer efficiency (LTE) overall.

This study proposed a new parameter, known as Void Index (VI), to quantify the voids underneath the slabs of thin concrete pavements. FWD deflections collected at the wheel path were used to determine the void index for different cells at different seasons. It was found that structural fibers can contribute to decreasing the voids underneath the slab, but a higher fiber dosage may be required for achieving such benefit.

This study developed two faulting prediction models for the ultra-thin and thin fiber reinforced concrete pavements constructed on a gravel base. Inputs such as slab thickness, base thickness,

modulus of subgrade reaction, residual strength of fiber reinforced concrete, void index, etc., can predict the faulting for a given ESAL.

While the synthetic structural fibers used in this study did demonstrate improvement to load transfer and mitigation of joint faulting, other factors such as constructability and cost must be considered when choosing such fibers. And while the fibers in this study slowed the development of joint faulting, it did not fully mitigate it. As this was essentially an accelerated experiment, further study should be conducted to determine whether the rate of faulting development for a given dosage or type of fiber would be acceptable for more typical low-volume traffic projects that would incorporate such thin designs.

REFERENCES

[1]. Byrum, C.R. and Perera, R.W., 2005. The effect of faulting on IRI values for jointed concrete pavements. In *Eighth International Conference on Concrete PavementsAmerican Association of State Highway and Transportation Officials (AASHTO) American Concrete Pavement AssociationCement Association of CanadaColorado Department of TransportationConcrete Reinforcing Steel InstituteFederal Highway AdministrationPortland Cement AssociationPurdue UniversityTransportation Research Board*.

[2]. ARA, Inc., ERES Division. *Guide for Mechanistic-Empirical Design of New and Rehabilitated Pavement Structure: Appendix JJ Transverse Joint Faulting Model.* National Cooperative Highway Research Program, Transportation Research Board, National Research Council, August 2003.

[3]. Simpson, A.L., J.B. Rauhut, P.R. Jordahl, E. Owusu-Antwi, M.I. Darter, and R. Ahmad. *Early Analysis of LTPP General Pavement Studies Data, Volume 3: Sensitivity Analyses for Selected Pavement Distresses, Report SHRP-P-393*, Strategic Highway Research Program, Washington, DC, 1994.

[4]. Yu, H.T., M.I. Darter, K.D. Smith, J. Jiang and L. Khazanovich. *Performance of Concrete Pavements Volume III - Improving Concrete Pavement Performance. Final Report, Contract DTFH61-91-C-00053*, Federal Highway Administration, McLean, VA, 1996

[5]. Wu, C.L., J.W. Mack, P.A. Okamoto, and R.G. Packard. *Prediction of Faulting of Joints in Concrete Pavements*, Proceedings, Fifth International Conference on Concrete Pavement Design and Rehabilitation, Vol. 2., Purdue University, West Lafayette, IN, April 1993.

[6]. Owusu-Antwi, E.B., L. Titus-Glover, L. Khazanovich, and J.R. Roesler. *Development and Calibration of Mechanistic-Empirical Distress Models for Cost Allocation.* Final Report, Federal Highway Administration, Washington, DC, March 1997.

[7]. Titus-Glover, L., E. Owusu-Antwi, and M I. Darter. *Design and Construction of PCC Pavements, Volume III: Improved PCC Performance. Report No. FHWA-RD-98-113*, Federal Highway Administration, Washington, DC, January 1999.

[8]. Hoerner, T.E., M.I. Darter, L. Khazanovich, L. Titus-Glover, and K.L. Smith. *Improved Prediction Models for PCC Pavement Performance-Related Specifications*, Volume I: Final Report, Publication No. FHWA-RD-00-130, August 2000.

[9]. Jung, Youn S., and Zollinger, Dan G. *New Laboratory-Based Mechanistic-Empirical Model For Faulting in Jointed Concrete Pavement*. Transportation Research Record: Journal of the Transportation Research Board, No. 2226, Transportation Research Board of the National Academies, Washington, D.C., 2011, pp. 60–70. DOI: 10.3141/2226-07

[10]. Chen, Y., and Lytton, Robert L. *Development of a New Faulting Model in Jointed Concrete Pavement using LTPP Data.* Transportation Research Record 2019, Vol. 2673(5) 407–417 National Academy of Sciences: Transportation Research Board 2019. DOI: 10.1177/0361198119838988

[11]. Khazanovich, L. Vandenbossche, Julie M., and Sachs, S., *Development of an Improved Design Procedure for Unbonded Concrete Overlays.* TPF-5 (269), Department of Civil and Environmental Engineering, University of Pittsburgh, November, 2019.

[12]. ASTM-C1609. (2010). Standard Test Method for Flexural Performance of Fiber-Reinforced Concrete (Using Beam With Third-Point Loading). American Society for Testing and Materials West Conshohocken, PA.

[13]. Barman, M. Crick. C., Roy, S., Tiwai, A., and Burnham, T. Performance Benefits of Fiber-reinforced Thin Concrete Pavement and Overlays. Task-2: Second Year Annual Cell Performance Report (2018-2019), MnDOT, St. Paul. MN.
[14]. MnDOT (2019). "MnROAD Semi Tractor Trailer". Minnesota Department of Transportation, St. Paul, MN. <http://www.dot.state.mn.us/mnroad/data/pdfs/MnROADSemiDescriptions(March%202013).pdf https://www.dot.state.mn.us/mnroad/data/traffic.html>
[15]. Deusen, Dave V., Burnhum, T., Dai S., Geib, J., Hanson, C., Izevbekhai, B., Johnson, E., Palek, L., Siekmeier, J., Vrtis,M., and Worel, B. *Report on 2017 MnROAD Construction Activities.* Report Number: MN/RC 2018-16. Minnesota Department of Transportation, May 2018.
[16]. Barman, M. and Hansen, B., 2018. Comparison of Performances of Structural Fibers and Development of a Specification for Using Them in Thin Concrete Overlays.
[17]. *Pavement Design Manual, Chapter 5*, Minnesota Department of Transportation, 2007.
[18]. ACPA website: http://apps.acpa.org/applibrary/KValue/
[19]. Crovetti, J., and Darter, M., *Void Detection for Jointed Concrete Pavement.* Transportation Research Record 1041, 1985 pp. 59-68.

APPENDIX

Table 9: ASTM C1609 test results

Specimen ID	MOR (psi)	Residual Strength Ratio (%)	Residual Strength (psi)
Cell 506-7day #1	465	-	-
Cell 506-7day #2		-	-
Cell 506-28day #1	650	-	-
Cell 606-7day #1	465	26.4	122.7
Cell 606-7day #2			
Cell 606-28day #1	635	19.4	124.1
Cell 606-28day #2			
Cell 706-7day #1	480	29.3	140.6
Cell 706-7day #2			
Cell 706-28day #1	675	23	156.4
Cell 706-28day #2			
Cell 806-7day #1	525	45.2	237.3
Cell 806-7day #2			
Cell 806-28day #1	680	37.4	254.3
Cell 806-28day #2			
Cell 139/239-28day #1	610	30.4	185.4
Cell 139/239-28day #2			
Cell 139/239-28day #3			
Cell 705/805-28day #1	542	21.5	116.5
Cell 705/805-28day #2			
Cell 705/805-28day #3			
Cell 705/805-28day #4			

Table 10: Properties of Concrete used in the NRRA cells

Fresh Concrete Properties								
Cell No.	139	239	705	805	506	606	706	806
Box Test	1,1,1,1	1,1,1,1	2,1,1,2	2,1,1,2	2,2,1,2	2,1,2,2	1,2,2,2	2,1,1,2
SAM No.	0.27	0.3	0.33	0.3	0.3	0.3	0.23	0.31
ASTM C231, Fresh air (%)	8.1	8.0	6.0	7.5	5.4	7.7	7.2	6.6
Hardened Concrete Properties								
Cell No.	139	239	705	805	506	606	706	806
Compressive strength, psi	1,910 (3 days)		2,990 (3 days)		2,740	2,360	2,690	2,510
	2,630 (7 days)		3,720 (7 days)		3,360	3,020	3,050	3,170
	3,800 (28 days)		- (28 days)		4,520	4,050	4,140	4,120
Surface resistivity 28 days, KW-cm	21.3		-		24.3	22.2	23.4	24.4
Air Content, %	8.3		-		5.8	8.5	6.3	6.5
Spacing factor, in.	0.0015		-		0.002	0.002	0.002	0.002

Specific surface, in2/in3	1,485	-	1,600	1,540	1,990	1,630
Dynamic Modulus of elasticity, 28 days	-	-	6.22 x 10^6 psi	5.21 x 10^6 psi	5.56 x 10^6 psi	4.97 x 10^6 psi
Poisson's Ratio	-	-	0.20	0.20	0.18	0.21
Static Modulus of Elasticity, 28 days	-	-	5.4 x 10^6 psi	4.3 x 10^6 psi	4.72 x 10^6 psi	4.61 x 10^6 psi

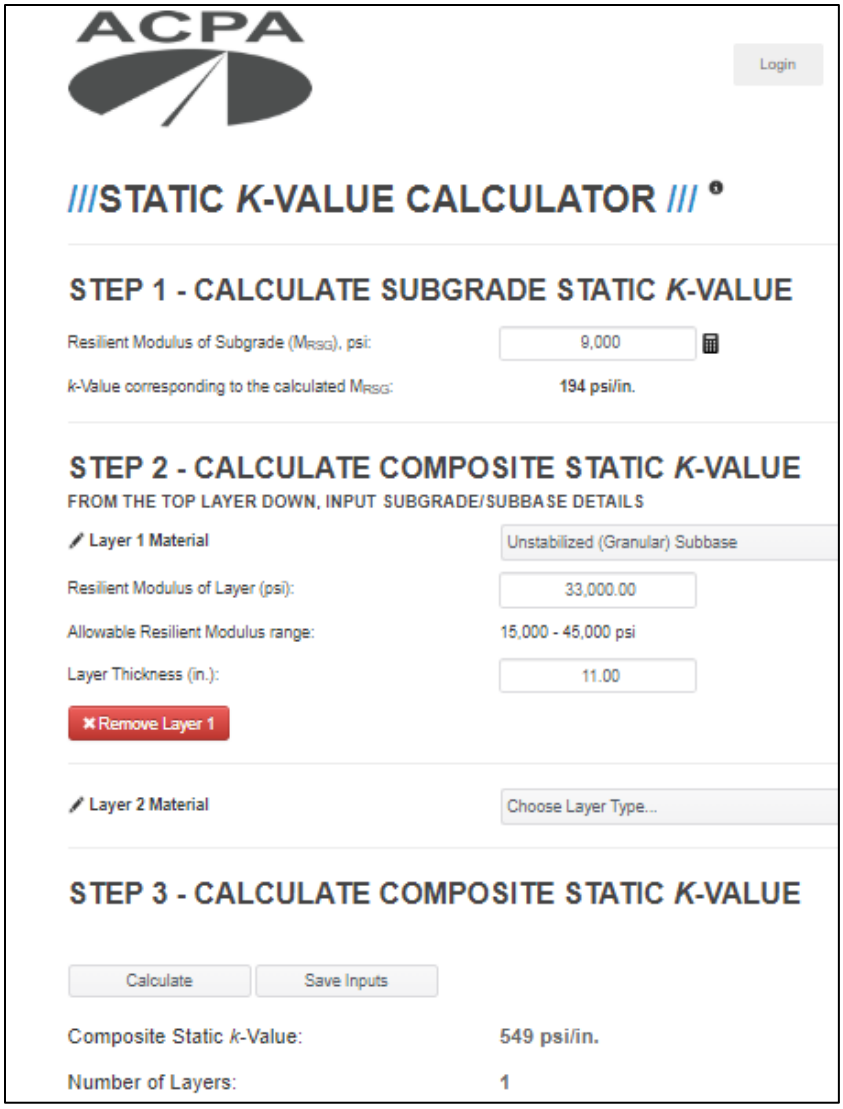

Figure 35: Combined modulus of subgrade reaction calculation